



VERIFICATION AND DEMONSTRATION OF EMBRACE AS A RADIO TELESCOPE TO OBSERVE ASTRONOMICAL SOURCES

Boudewijn Hut*

Under supervision of

Dr. ir. S.J. Wijnholds[‡], Prof. ir. A. van Ardenne^{‡§} and Prof. dr. J.M. van der Hulst*

Thursday 21st March, 2013

Abstract

The Electronic Multi-Beam Radio Astronomy ConcEpt (EMBRACE) is an Aperture Array (AA) which is developed as a pathfinder for the Square Kilometre Array (SKA) at ASTRON, designed to operate at the frequency range from 0.5 to 1.5 GHz. It has two stations, one in Nançay and one at the site of the Westerbork Synthesis Radio Telescope (WSRT). The WSRT station currently has 7056 antenna elements. The data processing of these elements is described in detail and based on this a number of verification measurements are developed to check the quality of the system. This testing is done by measurements on various sources like the Sun, satellites, galactic neutral hydrogen and other bright radio astronomical sources. The results show that the EMBRACE array is a system that can be used to do observations of astronomical sources. Consequently, AA technology, which is relatively new to radio astronomy, can in the future be used to do astronomically interesting observations in this frequency range.

*Kapteyn Astronomical Institute, University of Groningen, Groningen, The Netherlands

[‡]ASTRON, Netherlands Institute for Radio Astronomy, Dwingeloo, The Netherlands

[§]Chalmers University of Technology, Göteborg, Sweden

Table of Contents

1	Introduction	5
1.1	EMBRACE as a Demonstrator for SKA	5
1.2	Leiden-Dwingeloo Survey	7
1.3	This Thesis	7
2	Theory	9
2.1	Coordinate Systems	9
2.1.1	Cartesian Horizon Coordinate Systems: (x, y, z) and (l, m, n)	9
2.1.2	Spherical Horizon Coordinate Systems: (θ, ϕ) and (alt, az)	10
2.1.3	Equatorial Coordinate System: (α, δ)	10
2.1.4	Galactic Coordinate System: (ℓ, b)	10
2.1.5	Coordinate System for Array Aperture: (u, v, w)	13
2.2	Antenna Theory for Aperture Arrays	13
2.2.1	Array Factor	13
2.2.2	Element Factor	16
2.2.3	Resulting Antenna Pattern	18
3	EMBRACE Description	19
3.1	Data Processing	19
3.1.1	Analog Path	21
3.1.2	Digital Path	21
3.1.3	Frequency Selection Control	22
3.1.4	Control of Data Processing	22
3.2	Pointing the Array and Gain Calibrations	23
3.3	Filter Responses	24
3.3.1	Filter Response for Data Transfer	24
3.3.2	Filter Response per Subband	24
3.3.3	Correction to the Digital Filter Response	27
3.4	Performance of an Expanding Array	28
3.4.1	Frequency Measurements of a Geostationary Satellite	28
4	Fringe Measurements	31
4.1	Correlations and Fringe Measurements	31
4.2	Fringe Measurements on Stars and Satellites	34
4.3	Correlator Offset and Correction	37

5	System Temperature of EMBRACE	39
5.1	T_{sys} Determination by Fringe Measurements on Cassiopeia A	39
5.2	T_{sys} Determination by Spectra from Galactic HI	40
5.2.1	Spectra of Galactic HI by the Leiden-Dwingeloo Survey	41
5.3	Comparison of Results for T_{sys}	42
6	Observing Astronomical Sources	43
6.1	Tile and Array Beams	43
6.2	Integration Time and Sensitivity	44
6.3	Convolution of Leiden-Dwingeloo Survey Data	45
6.4	Spectra by EMBRACE	47
6.4.1	Data Reduction	47
7	Conclusions and Future Work	49
7.1	Future Work	49
8	Acknowledgements	51
	References	53
	Glossary	55

This project is done as part of the master Astronomy at the University of Groningen, in cooperation with Netherlands Institute for Radio Astronomy (ASTRON). ASTRON is part of the Netherlands Organisation for Scientific Research (NWO).



university of
 groningen

faculty of mathematics
 and natural sciences

kapteyn astronomical
 institute

ASTRON

Netherlands Institute for Radio Astronomy

NWO

Netherlands Organisation for Scientific Research

Chapter 1

INTRODUCTION

When the Square Kilometre Array (SKA) is fully operational in 2024, it will be the biggest radio telescope of the world (SKA Organisation 2013). It will be a telescope that will bring revolution in astronomy, since this telescope will provide about a million square metres of collecting area for a continuous frequency coverage from 50 MHz to 20 GHz. SKA will consist of three types of telescopes, depending on the frequency range. There will be dish telescopes for frequencies from 350 MHz to 20 GHz, SKA-mid/AA with mid frequency Aperture Arrays (AA) for frequencies from 400 MHz to 1.5GHz and SKA-low with low frequency AA's for the frequencies from 50 to 450 MHz. Astronomers and engineers around the world are now working on the instrument design and technology that will be used for the different frequency ranges. The Netherlands Institute for Radio Astronomy (ASTRON) is working on the AA technology that can be used in SKA-mid and SKA-low.

1.1 EMBRACE as a Demonstrator for SKA

As part of a series of demonstrator telescopes towards SKA, ASTRON is now working on the development of the Electronic Multi-Beam Radio Astronomy ConcEpt (EMBRACE). This operational telescope will demonstrate the use of independent, multiple, wide field and wide band receiving antenna beams. EMBRACE has two stations: one in Nançay, France and another at the site of the Westerbork Synthesis Radio Telescope (WSRT) in The Netherlands.

The biggest one will be at the WSRT site and will consist of 144 tiles with 72 antenna elements in a single polarization, providing a collecting area of ~ 150 square metres. The results of the first 10% of the tiles showed that the data path works and revealed the system temperature at 1 GHz to be somewhere between 103 K and 117 K (Wijnholds et al. 2009), which is quite close to the desired 100 K (Kant et al. 2011). EMBRACE has two analog, independent beams per tile and this tile beam can contain max 8 smaller digital array beams, see Figure 1.1 (*left*). This and the other main requirements are listed in Table 1.1.

During the time this thesis work took place, the size of the WSRT station was expanded to 68% of its total station size and the back-end was updated as well. Figure 1.1 (*right*) shows the front-end of EMBRACE. It is dual polarization, but only a single polarization is connected to the back-end to reduce costs. So only a single polarization of the waves can be detected. Furthermore, the focus of this thesis will be on a single analogue beam only.

<i>Requirement</i>	<i>Remark</i>	<i>Value</i>
Number of stations	in Nançay and Westerbork	2
Total physical collecting area	both stations	300 m ²
Aperture efficiency		≥ 0.8
System Temperature	at 1 GHz	≤ 100 K
Frequency range		500 - 1500 MHz
Instantaneous array bandwidth	RF beam	100 MHz
Number of analogue FoVs	RF beam	2
Half Power Beam Width	RF beam at 1 GHz	$> 15^\circ$
Scan range θ	from zenith	$\geq 45^\circ$
Side lobe levels	w.r.t. main beam, no grating lobes	≤ -13.2 dB
Number of digital beams	per FoV	≥ 8

Table 1.1: EMBRACE demonstrator main requirements (Kant et al. 2011).

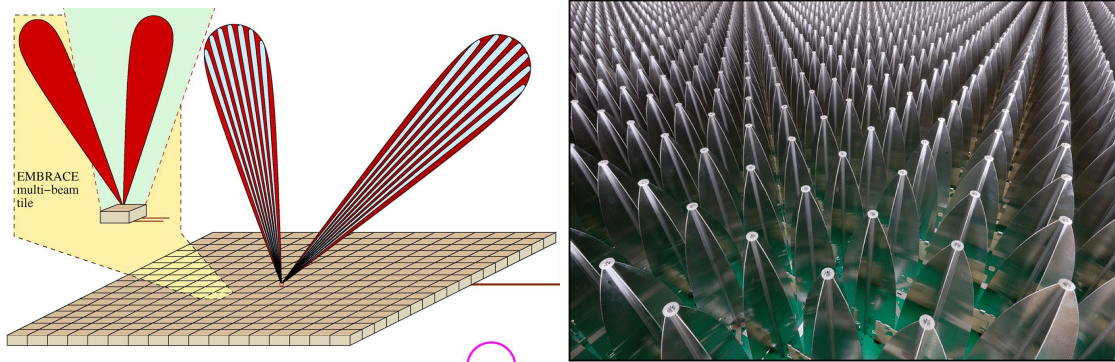


Figure 1.1: (left) Illustration of two analog beams with 8 digital beams (right) The antenna elements in the front-end of EMBRACE. Images from (Kant et al. 2011).

1.2 Leiden-Dwingeloo Survey

While the EMBRACE array at the WSRT site is getting to its final dimensions, it is becoming more competitive to conventional dishes in terms of sensitivity. A big advantage of dishes is that their beam shape do not change with pointing. Due to mechanical motors, their beam is always optimal for the direction of observation. This is not the case in AA telescopes, which relies on electronic pointing only. On the other hand, conventional dishes can only make a single beam during an observation. AA technology allows to make multiple beams simultaneously, with corresponding increase of the survey speed. So the fundamentals of AA technology differ from the ones of conventional dishes.

As such, it is important to make a comparison between the results from both technologies. Something that is observed in detail with dishes is the emission of atomic hydrogen (HI). It is the main tracer of the interstellar medium in the Milky Way. This emission has a rest frequency of $f_{HI} = 1420.41$ MHz and a corresponding wavelength $\lambda_{HI} = 0.211061$ m. Figure 1.2 shows a map of the distribution of this emission, which has been taken from the Leiden-Dwingeloo Survey (LDS) data. The LDS data were measured over a five year period with the 25-meter Dwingeloo Telescope and were published in 1997 (Hartmann and Burton 1997). It used a grid in the galactic plane on every 85% half-power beam width (HPBW), which corresponds to 60% from the Nyquist sampling theorem. At 1420 MHz, the HPBW of the Dwingeloo Telescope is 0.6° . The unit of the frequency axis in the LDS data is velocity with respect to the local standard of rest v_{lsr} , with resolution of $\Delta v_{lsr} = 1.03$ km s $^{-1}$.

1.3 This Thesis

The availability of the LDS data in combination with the presence of the EMBRACE WSRT station results in the following research question:

Can AA technology produce data of scientific quality at the SKA mid/AA frequencies?

When the data from AA technology is represented by data from the EMBRACE WSRT station, then this question could be answered by comparing EMBRACE observations with LDS data. To do so, it will be needed to study the EMBRACE WSRT station in detail first.

The outline of this thesis follows this structure. First some AA fundamentals are presented and afterwards the general EMBRACE system is discussed and some instrumental effects are assessed. EMBRACE is used in chapter 4 to perform fringe measurements, which are used in chapter 5 to find the system temperature of EMBRACE. Chapter 6 presents a way to map astronomical sources. Finally, the conclusions from all this and suggested future work conclude this thesis.

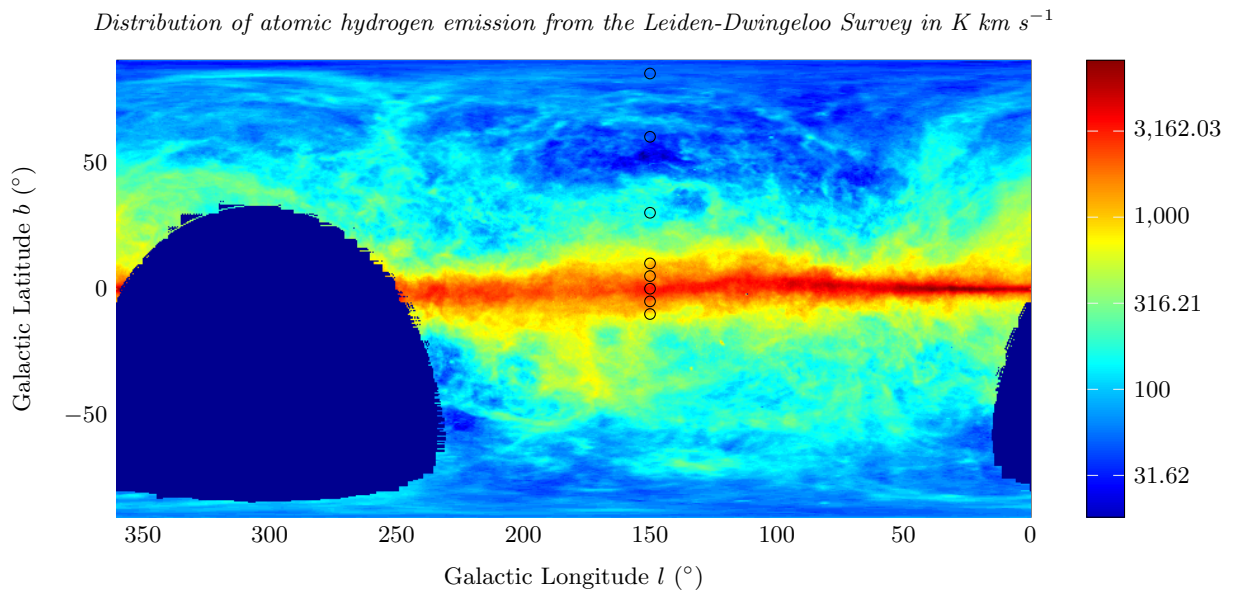


Figure 1.2: Distribution of atomic hydrogen emission from the LDS, integrated over $-450 \leq v_{lsr} \leq 400 \text{ km s}^{-1}$ (Hartmann and Burton 1997). This corresponds to integration over frequency from $f = 1.41823$ to $f = 1.4224 \text{ GHz}$, in steps of width $\Delta f = 4.880 \text{ kHz}$. The coordinates of the black circles correspond to the spectra in Figure 5.2. The dark blue areas correspond to galactic coordinates that are not visible from Dwingeloo.

Chapter 2

THEORY

The elements of EMBRACE are sensitive to radiation from every direction. This chapter explains how the responses of the elements are combined to do astronomical observations. First there will be a discussion about coordinate systems and then about the principles of AA technology.

2.1 Coordinate Systems

Astronomical observations always involve transformations between different coordinate systems. The positions of the telescope elements are expressed in a Cartesian system, while the positions on the sky is in a horizon system. Furthermore, the astronomical sources are often expressed in equatorial or galactic coordinates.

2.1.1 Cartesian Horizon Coordinate Systems: (x, y, z) and (l, m, n)

The element locations of EMBRACE are defined in a local (x, y, z) Cartesian coordinate system and sources on the sky are located in a normalized (l, m, n) one. Accordingly, the units in the (x, y, z) system are meters and the (l, m, n) system is unitless. Both systems are based on the quarters of the compass on the same way.

$$\left\{ \begin{array}{l} l \\ m \\ n \end{array} \right. \begin{array}{l} \text{East - West direction (East positive)} \\ \text{North - South direction (North positive)} \\ \text{nadir - zenith direction (zenith positive)} \end{array} \quad \left\{ \begin{array}{l} x \\ y \\ z \end{array} \right. \begin{array}{l} \parallel \hat{e}_l \\ \parallel \hat{e}_m \\ \parallel \hat{e}_n \end{array}$$

Cartesian and spherical horizon coordinates systems on Earth at the position of an observer

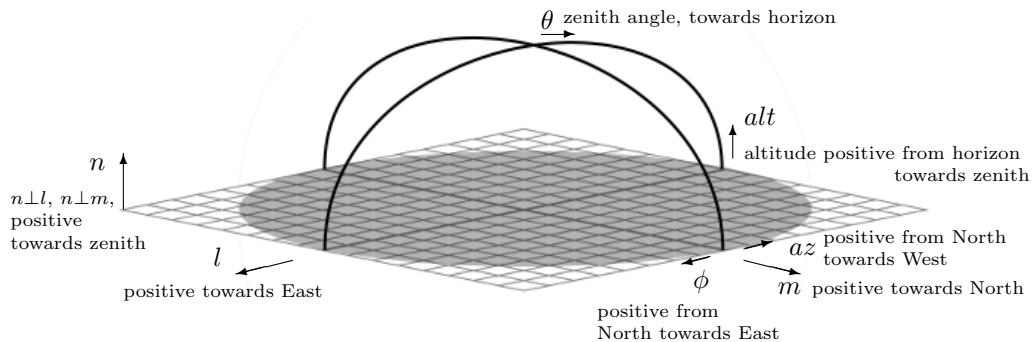


Figure 2.1: Cartesian and horizon coordinate systems.

2.1.2 Spherical Horizon Coordinate Systems: (θ, ϕ) and (alt, az)

From the (l, m, n) coordinate system, conversions can be made to a spherical horizon coordinate system. For a position on the sky P , the angle between zenith and P is given by the zenith angle θ . The azimuth angle ϕ is the angle parallel to the horizon from North to P (East positive). The transformations are given by

$$\begin{cases} \theta & \text{Angle between zenith and source} \\ \phi & \text{Angle between North and source (East positive)} \end{cases} \Rightarrow \begin{bmatrix} l \\ m \\ n \end{bmatrix} = \begin{bmatrix} \sin(\theta) \cos(\phi) \\ \sin(\theta) \sin(\phi) \\ \cos(\theta) \end{bmatrix}. \quad (2.1)$$

The coordinates are sometimes given in another spherical horizon system. In the (alt, az) system is the altitude angle alt given by the distance between the horizon and P . The az angle is also an azimuth angle, now measured from North to P (West positive):

$$\begin{cases} \theta = 90^\circ - alt \\ \phi = -az \end{cases} \Rightarrow \begin{bmatrix} l \\ m \\ n \end{bmatrix} = \begin{bmatrix} \cos(alt) \cos(az) \\ -\cos(alt) \sin(az) \\ -\sin(alt) \end{bmatrix}. \quad (2.2)$$

2.1.3 Equatorial Coordinate System: (α, δ)

The coordinate systems until now are attached to a position on Earth. Because of the rotation of the Earth, the transformation to the equatorial coordinate system with the Sun as its center, includes the time of observation. The hour angle h of a source is given by the local sidereal time (LST) and the right ascension α of the source, e.g.

$$h = \text{LST} - \alpha. \quad (2.3)$$

For an observer at a geometrical latitude lat , the transformation is then given by

$$\begin{cases} \delta = \arcsin(\sin(alt) \sin(lat) + \cos(alt) \cos(lat) \cos(az)) \\ \alpha = \text{LST} - \arccos\left[\frac{\sin(alt) - \sin(\delta) \sin(lat)}{\cos(\delta) \cos(lat)}\right] \end{cases}. \quad (2.4)$$

Or in matrix notation, using the (l, m, n) coordinate system to apply transformations to get a $\mathbf{s}_{\alpha, \delta}$ in Cartesian representation (Green 1993),

$$\mathbf{s}_{\alpha, \delta} = \begin{bmatrix} \cos(LST) & -\sin(LST) & 0 \\ \sin(LST) & \cos(LST) & 0 \\ 0 & 0 & 1 \end{bmatrix} \begin{bmatrix} \cos(lat) & 0 & -\sin(lat) \\ 0 & 1 & 0 \\ \sin(lat) & 0 & \cos(lat) \end{bmatrix} \begin{bmatrix} 0 & 0 & 1 \\ 1 & 0 & 0 \\ 0 & 1 & 0 \end{bmatrix} \begin{bmatrix} l \\ m \\ n \end{bmatrix}. \quad (2.5)$$

Where $\mathbf{s}_{\alpha, \delta}$ is the position vector

$$\mathbf{s}_{\alpha, \delta} = \begin{bmatrix} \cos(\alpha) \cos(\delta) \\ \sin(\alpha) \cos(\delta) \\ \sin(\delta) \end{bmatrix}. \quad (2.6)$$

In this representation it is easier to apply corrections for nutation. During this research, no extra corrections have been applied, because the sizes of the array beam is still too large to have effect. The units of all quantities should be converted to degrees or radians. The LST can be calculated according to the Julian date JD by means of (alm 2012).

2.1.4 Galactic Coordinate System: (ℓ, b)

The original definitions for the galactic coordinate system are threefold. First of all, the North Galactic Pole (NGP) lies in the equatorial system (J2000 epoch) in the direction of

$$\begin{bmatrix} \alpha \\ \delta \end{bmatrix}_{\text{NGP}} = \begin{bmatrix} 12^\circ.8567 \\ 27^\circ.13 \end{bmatrix}. \quad (2.7)$$

Besides, the zero of galactic latitude b is the great semicircle originating 90° away from the NGP at the position angle of 123° with respect to the equatorial pole. And finally the galactic longitude goes from zero to 360° , in the same fashion as the right ascension on the galactic equator (Blaauw et al. 1959). The galactic latitude b goes from -90° at the South Galactic Pole to $+90^\circ$ at NGP. Using the equatorial coordinates of the galactic center (GC),

$$\begin{bmatrix} \alpha \\ \delta \end{bmatrix}_{\text{GC}} = \begin{bmatrix} 17.^\circ 76 \\ -28.^\circ 94 \end{bmatrix}, \quad (2.8)$$

it is possible to rewrite the equatorial system into the galactic system by using

$$\mathbf{s}_{b,\ell} = \mathbf{R} \cdot \mathbf{s}_{\alpha,\delta}. \quad (2.9)$$

Here $\mathbf{s}_{\alpha,\delta}$ is the position on the equatorial sphere and $\mathbf{s}_{b,\ell}$ is the corresponding position on the galactic sphere,

$$\mathbf{s}_{b,\ell} = \begin{bmatrix} \cos(\ell) \cos(b) \\ \sin(\ell) \cos(b) \\ \sin(b) \end{bmatrix}. \quad (2.10)$$

\mathbf{R} is the rotation matrix, it contains the positions of NGP and GC:

$$\mathbf{R} = \begin{bmatrix} \mathbf{s}_{GC} & \mathbf{s}_{GC} \times \mathbf{s}_{NGP} & \mathbf{s}_{GC} \end{bmatrix}, \quad (2.11)$$

where \mathbf{s}_{NGP} and \mathbf{s}_{GC} are the $\mathbf{s}_{\alpha,\delta}$ vectors for the coordinates in respectively Equations (2.7) and (2.8). Combining Equations (2.6), (2.9) and (2.10) will give the coordinates ℓ , b by the arctan of the first over the second entry and by the arcsin of the third entry of $\mathbf{s}_{b,\ell}$ (Green 1993).

The coordinate systems that are discussed can be used to do the transformations. An example of the sky on 1 February 2013 in the different representations is shown in Figure 2.2.

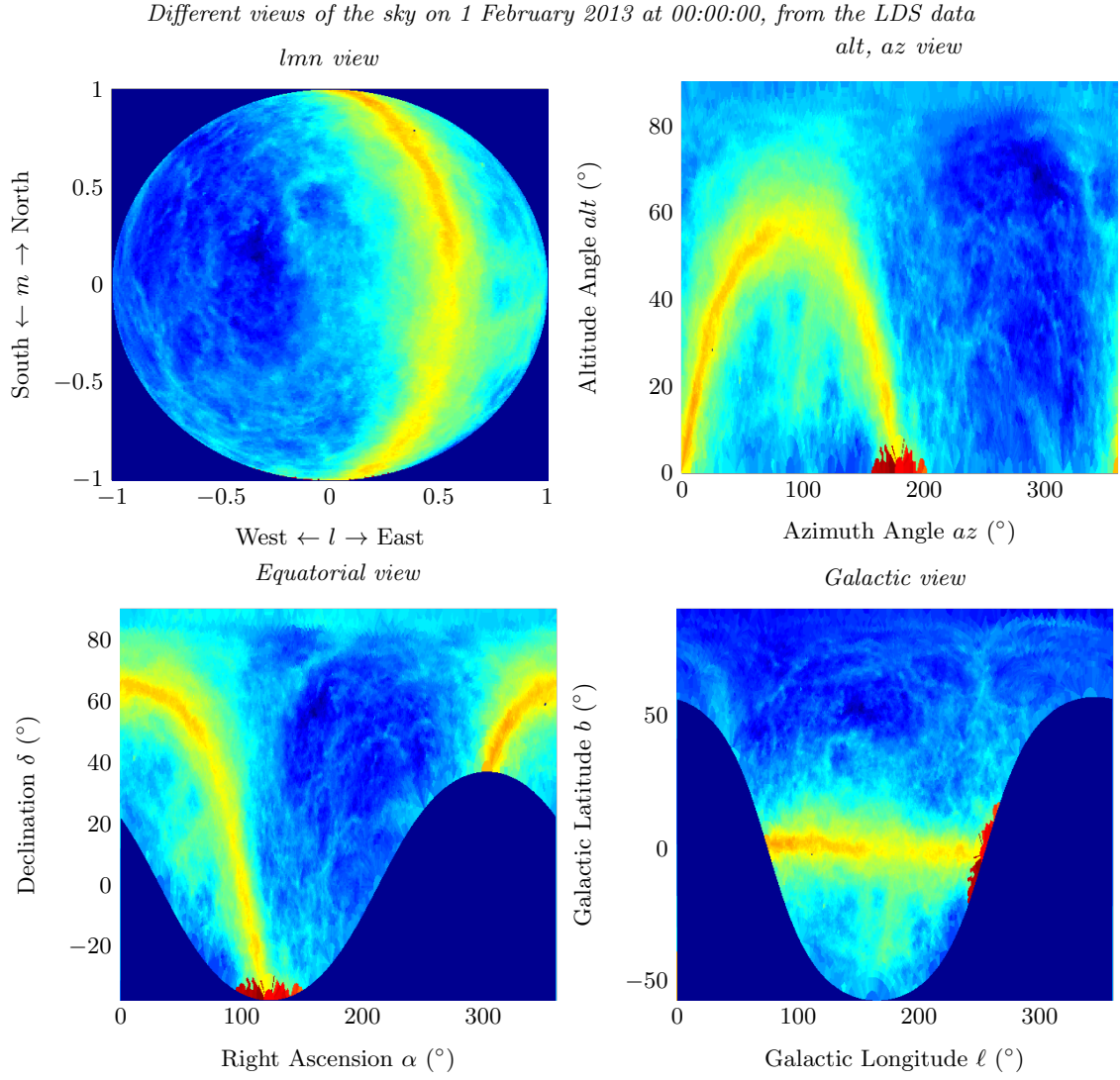


Figure 2.2: The sky on 1 February 2013 at 00:00:00 presented in different coordinate systems, calculated by the transformations given in this chapter.

2.1.5 Coordinate System for Array Aperture: (u, v, w)

Another Cartesian coordinate system that is used in radio astronomy is the (u, v, w) coordinate system. It is used to express baseline vectors. It is defined according to the North Pole and East and depends on the position of the source that is observed. This coordinate system should not be confused with the (l, m, n) or (x, y, z) coordinate systems.

$$\begin{cases} u & \text{East - West direction (East positive)} \\ v & \text{towards North Pole} \\ w & \text{towards source on the sky} \end{cases} \quad (2.12)$$

For a pointing to zenith, $u \parallel x$, $v \parallel y$ and $w \parallel z$.

2.2 Antenna Theory for Aperture Arrays

In an AA system like EMBRACE, the responses of multiple elements are combined to improve the overall sensitivity. The Antenna Pattern (AP, or sometimes radiation pattern RP) is the distribution of flux at distances where the field can be approximated by a planar wave (Burke and Graham-Smith 2010). This approximation can be made when the distance R to the source is such that one can speak of the far field. That is when the baseline length d and the wavelength λ relate to the distance R by

$$R \geq \frac{d^2}{\lambda}. \quad (2.13)$$

So astronomical sources are always in the far field. The AP is the result of the pattern multiplication between the Array Factor AF and the Element Factor EF,

$$\text{AP}(\theta, \phi) = \text{AF}(\theta, \phi) \cdot \text{EF}(\theta, \phi). \quad (2.14)$$

This makes it possible to separate the two effects that make the AP: first of all the effect of the position of each element within the array and secondly the sensitivity to radiation of the elements. It should be noted that Equation (2.14) is only valid for identical elements. This means that the sensitivity to radiation for every element should be the same. It is known that this is not valid for AAs in general: elements that are placed along the edge of an array behave electrically different from elements that are surrounded by other elements. For small arrays Equation (2.14) may not be valid, but for larger arrays the assumption that all elements behave the same way becomes fine. That is because in a rectangular array, the number of elements that are surrounded by others relates quadratically to the total number of elements in the array, while the number of elements that are on an edge relates only linear. For large arrays like EMBRACE, the total number of elements will be dominated by elements that are surrounded by other elements. The two factors that are in Equation (2.14) will be discussed in the following subsections.

2.2.1 Array Factor

Each element in an array has a different position. As such, they all will have a specific geometrical delay as depicted in Figure 2.3. For a two-dimensional array with M elements in the x direction and N elements in the orthogonal y direction, these geometrical phase delays can be put in a vector \mathbf{w} ,

$$\mathbf{w} = \begin{bmatrix} w_1 \\ w_2 \\ \vdots \\ w_{MN} \end{bmatrix}, \quad (2.15)$$

where the individual phase delays are given by

$$w_n = e^{i\mathbf{k}_0 \cdot \mathbf{r}_n} \quad (2.16)$$

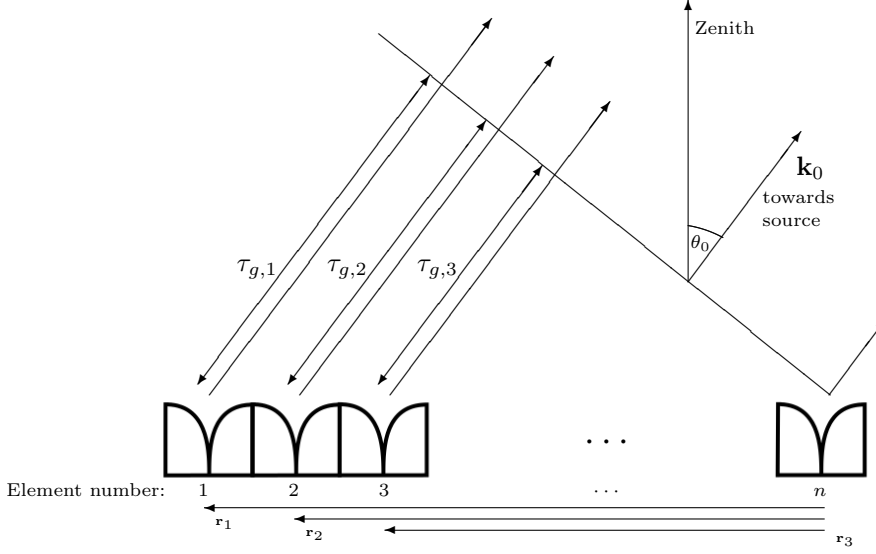


Figure 2.3: The geometrical delay is different for each element, depending on the incident wave vector \mathbf{k}_0 and on the position \mathbf{r}_n of the element.

where n is the element index $1 \leq n \leq MN$. Here the pointing of the array is towards the wave with wavevector \mathbf{k}_0 and comes from a source at (θ_0, ϕ_0)

$$\mathbf{k}_0 = \begin{bmatrix} k_x \\ k_y \\ k_z \end{bmatrix} = \frac{2\pi}{\lambda} \begin{bmatrix} \sin \theta_0 \cos \phi_0 \\ \sin \theta_0 \sin \phi_0 \\ \cos \theta_0 \end{bmatrix} = \frac{2\pi}{\lambda} \begin{bmatrix} l \\ m \\ n \end{bmatrix}. \quad (2.17)$$

The vector \mathbf{r}_n represents a unit signal from the positions of the elements that are in the array

$$\mathbf{r}_n = \begin{bmatrix} x_n \\ y_n \\ z_n \end{bmatrix}. \quad (2.18)$$

If then $\mathbf{v}(\mathbf{k})$ represents the unit signal on the sky that we want to observe, e.g.

$$\mathbf{v}(\mathbf{k}) = \begin{bmatrix} e^{-i\mathbf{k}\cdot\mathbf{r}_1} \\ e^{-i\mathbf{k}\cdot\mathbf{r}_2} \\ \vdots \\ e^{-i\mathbf{k}\cdot\mathbf{r}_{MN}} \end{bmatrix}, \quad (2.19)$$

then the antenna factor AF is defined as

$$\text{AF} = \mathbf{w}^\top \cdot \mathbf{v}(\mathbf{k}). \quad (2.20)$$

To make a map of the sky for a pointing towards (θ_0, ϕ_0) , AF may be explicitly stated as function of beam pointing direction (θ_0, ϕ_0) and probe location (θ_p, ϕ_p)

$$\text{AF}(\theta_0, \phi_0, \theta_p, \phi_p) = \mathbf{w}^\top(\theta_0, \phi_0) \cdot \mathbf{v}(\theta_p, \phi_p). \quad (2.21)$$

For some array configurations AF is calculated. Figure 2.4 shows some configurations that are or will be realized by EMBRACE. It is this $\text{AF}(\theta_0, \phi_0, \theta_p, \phi_p)$ that will be used to make the antenna pattern AP by calculating this for all possible values of θ_p and ϕ_p .

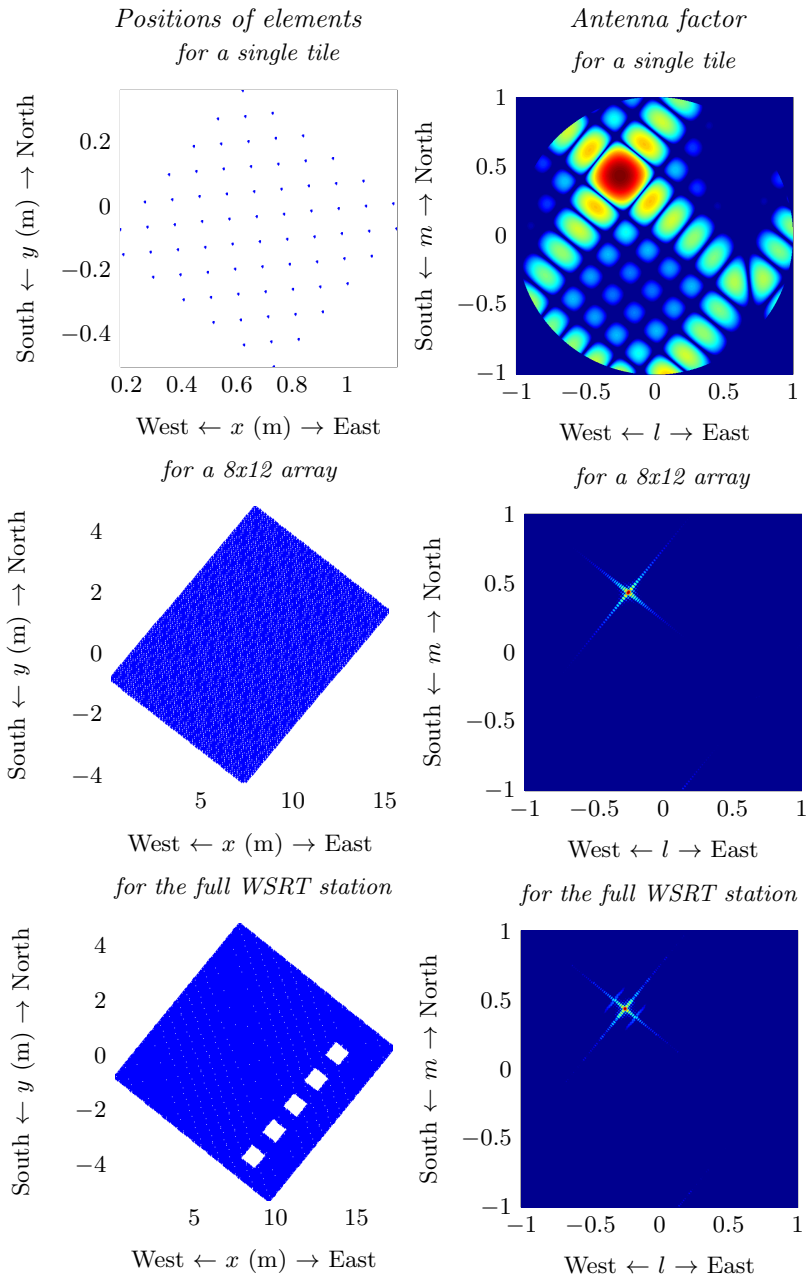


Figure 2.4: Calculated array factors (*right*) for a pointing towards $(\theta_0, \phi_0) = (30^\circ, 330^\circ)$ or $(l, m, n) = (-0.250, 0.433, 0.866)$ and for different array configurations (*left*): (*first row*) a single tile; (*second row*) 8×12 tiles; (*third row*) 12×12 tiles.

2.2.2 Element Factor

To make a map of the AP, the element factor EF should also be known. Data from previous experiments were made available. The simulation was done for all elements on a single tile and the data that were provided, contained per element the complex gain as a result of the excitation from an incident, polarized wave. Moreover, the complex gain per element was given for a specific frequency, a specific source position on the sky and done for both polarizations (Φ and Θ) of the incident wave. So let the vector \mathbf{e} represent the incident wave and let its elements e_Θ and e_Φ represent the contribution in the corresponding polarization,

$$\mathbf{e} = \begin{bmatrix} e_\Theta \\ e_\Phi \end{bmatrix}. \quad (2.22)$$

This wave will be received by an element with complex gains \mathbf{G} ,

$$\mathbf{G} = \begin{bmatrix} g_{\Theta,l} & g_{\Phi,l} \\ g_{\Theta,m} & g_{\Phi,m} \end{bmatrix}, \quad (2.23)$$

where the subscripts represents the gain in the orthogonal l or m polarization with respect to the Θ contribution of the incident wave and similiary for the Φ component of the incident wave. This is chosen such that the sensitivity of an element is given by \mathbf{b} ,

$$\mathbf{b} = \begin{bmatrix} b_l \\ b_m \end{bmatrix} = \mathbf{G}\mathbf{e} = \begin{bmatrix} g_{\Theta,l} & g_{\Phi,l} \\ g_{\Theta,m} & g_{\Phi,m} \end{bmatrix} \begin{bmatrix} e_\Theta \\ e_\Phi \end{bmatrix}. \quad (2.24)$$

So the values for $g_{\Theta,l}$, $g_{\Phi,l}$, $g_{\Theta,m}$ and $g_{\Phi,m}$ are provided for every element in the array, for frequencies from 300 to 1400 MHz (in steps of 25 MHz) and for a grid in spherical horizon coordinates defined by θ and ϕ : θ goes from 0° to 180° and ϕ goes from 0° to 360° , both in steps of 5° . To get an EF from this, it is assumed that all elements are identical and behave the same way. Consequently, the two most central elements are combined by the mean of their data values as an approximation to a get a generic element factor. Since EMBRACE can measure only a single polarization of the incoming waves, the total power of the elements can be used to make the EF. The total power is given by $\mathbf{P} = \mathbf{b}\mathbf{b}^H$, so

$$\mathbf{P} = \mathbf{b}\mathbf{b}^H = \mathbf{G}\mathbf{e}(\mathbf{G}\mathbf{e})^H = \mathbf{G}\mathbf{e}\mathbf{e}^H\mathbf{G}^H = \mathbf{G}(\mathbf{e}\mathbf{e}^H)\mathbf{G}^H, \quad (2.25)$$

where \mathbf{G}^H denotes the Hermitian conjugate of the matrix \mathbf{G} . For the factor $\mathbf{e}\mathbf{e}^H$,

$$\mathbf{e}\mathbf{e}^H = \begin{bmatrix} e_\Theta e_\Theta & e_\Theta e_\Phi \\ e_\Phi e_\Theta & e_\Phi e_\Phi \end{bmatrix} = E_0 \begin{bmatrix} 1 & 0 \\ 0 & 1 \end{bmatrix}, \quad (2.26)$$

where the last equal sign is for an unpolarized incident wave. This is valid for the test, thus Equation (2.25) can be rewritten to

$$\mathbf{P} = E_0 \mathbf{G}\mathbf{G}^H \quad (2.27)$$

and $E_0 = 1$ can be assumed. Because the elements of EMBRACE can only detect a single polarization of the incident wave, the element factor is given by \mathbf{P}_{ll} , e.g.

$$\text{EF}(\theta, \phi) = g_{\Theta,l}g_{\Theta,l}^* + g_{\Phi,l}g_{\Phi,l}^*. \quad (2.28)$$

The provided data and the resulting EF is shown in Figure 2.5.

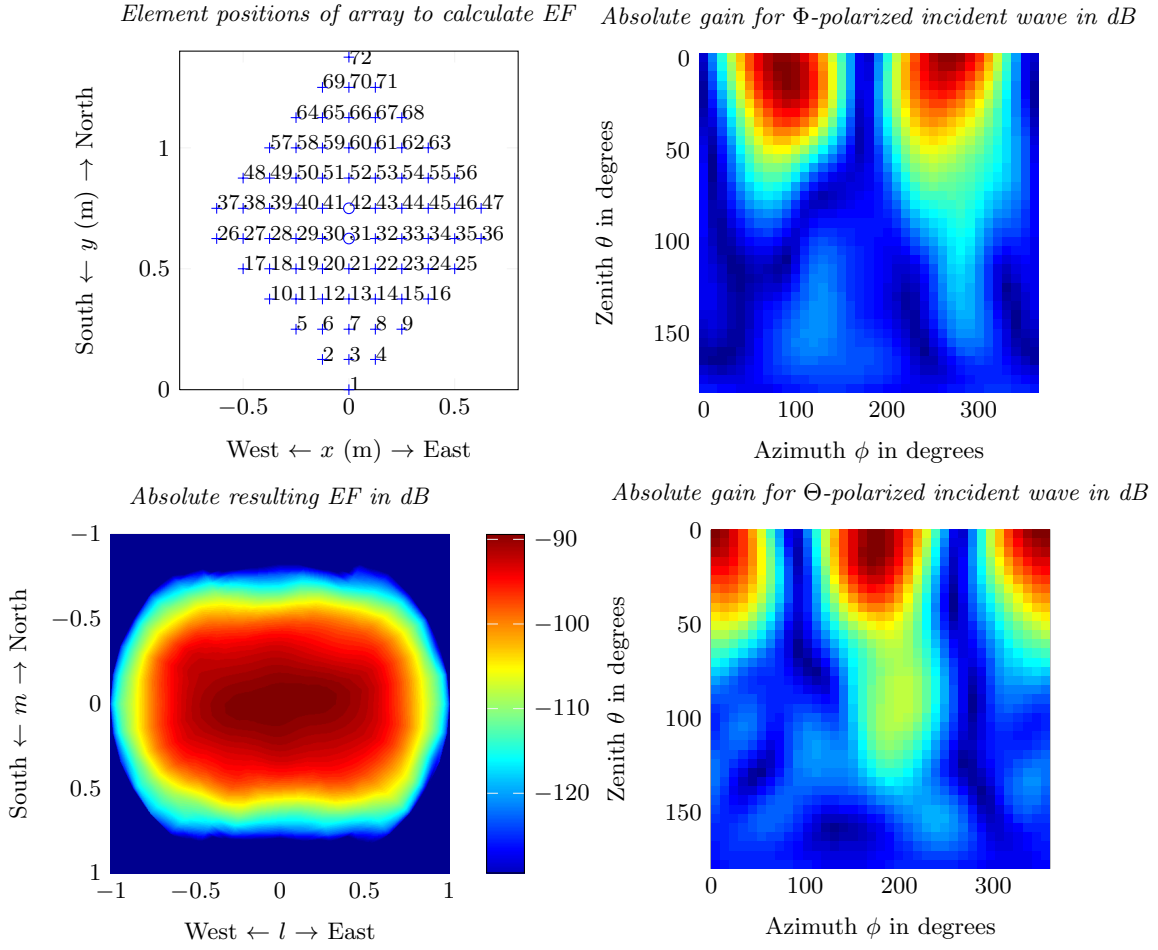


Figure 2.5: (top, left) The numbered elements in the l polarization for the EF determination. (right) The absolute values of the provided complex gains for different polarizations of the incident wave: (top) Φ polarized; (bottom) Θ polarized. (bottom, left) The determined EF by using the central elements with number 31 and 42.

2.2.3 Resulting Antenna Pattern

In the previous sections the antenna factor and element factor were calculated and by Equation (2.14), the resulting antenna pattern can be calculated but also needs to be normalized correctly. When one considers the array to be an emitter*, then the energy that is put in the transmitter will come through a surface that encloses the array. The emitted energy will be mainly in the main lobe, unless the side lobes become more significant. For example when the beam in Figure 2.4 is pointed more towards the horizon, then the contribution of the side lobe will equal the contribution of the main lobe due to the attenuation of the EF. If there is no normalization, the emitted energy will be more than the available energy and this would be a violation of the law of conservation of energy. So the result of the pattern multiplication should be normalized by the total energy that goes through the enclosing surface:

$$AP(\theta_0, \phi_0, \theta, \phi) = \frac{AF(\theta_0, \phi_0, \theta, \phi) \cdot EF(\theta, \phi)}{\int_{\Omega} AF(\theta_0, \phi_0, \theta, \phi) \cdot EF(\theta, \phi) d\Omega} = \frac{AF(\theta_0, \phi_0, \theta, \phi) \cdot EF(\theta, \phi)}{\int_{-\frac{1}{2}\pi}^{\frac{1}{2}\pi} \int_0^{2\pi} AF(\theta_0, \phi_0, \theta, \phi) \cdot EF(\theta, \phi) \sin(\theta) d\theta d\phi}. \quad (2.29)$$

Figure 2.6 shows the result for AP.

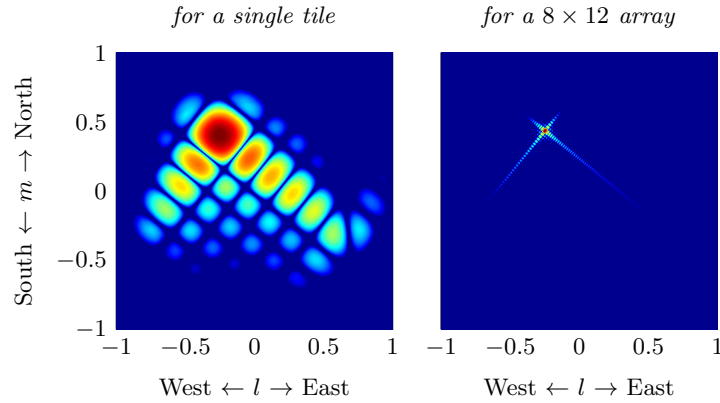


Figure 2.6: Calculated antenna patterns as the normalized pattern multiplication between EF from Figure 2.5 and AF from (left) a single tile (see Figure 2.4 (top, right)) and (right) a 12×9 configuration (see Figure 2.4 (second row, right)).

*By the reciprocity principle, the radiation pattern will be the transmission pattern.

Chapter 3

EMBRACE DESCRIPTION

The EMBRACE system is a system with many antenna elements. All the data in the 500 MHz bandwidth that is produced by the antenna elements need to be processed. This chapter is about how that is done. The first section is about the analog and digital data paths and how to control them. This control is used for the calibration of the array in the third section. After that, instrumental effects like filter responses are discussed in section 3.3. A general check of the WSRT station is performed in the final section.

3.1 Data Processing

The induced voltages in the elements are first processed by analog electronics and then converted to the digital domain. As such, the first subsection is about the analog data path and the second about the digital path. A complete overview is given in Figure 3.1.

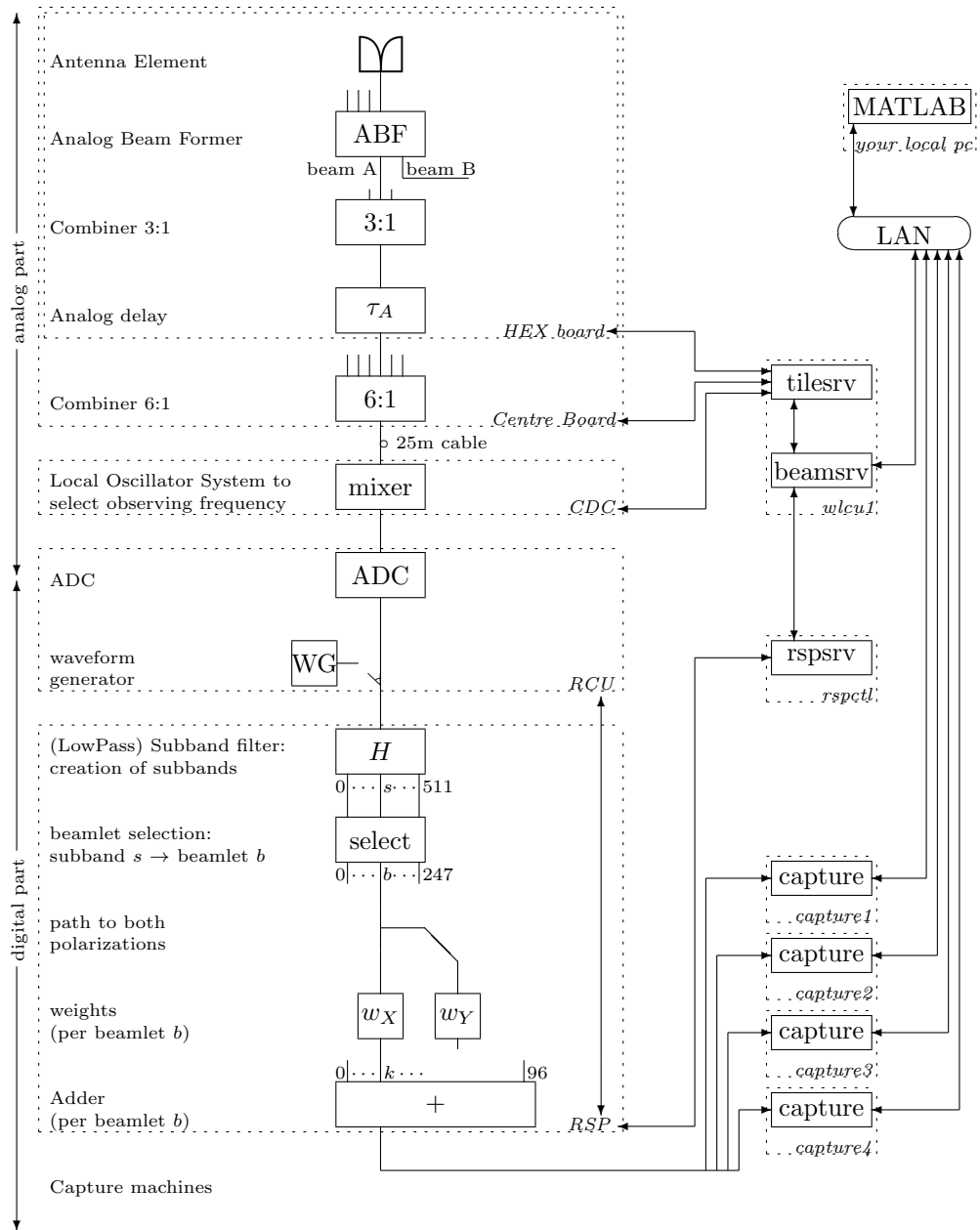


Figure 3.1: Simplified signal path for a signal from an antenna element and its control.

3.1.1 Analog Path

The induced voltages of four elements are beamformed by an analog beamformer, before the distinction can be made between the independent A and B beams. Since the processing of the independent beams are in essence the same, only the A beam will be discussed here. The physical separation of the A and B beam needs to be done quite early in the chain, such that the geometrical delays can be applied separately. These delays are applied on the HEX board, just after the signal of three analog beamformers are added. This signal is passed to the Centre Board, on which the signals from the 6 HEX boards are added. There is one Centre Board per tile, so the output of this board will be the ‘tile beam’. After transferring this signal over a 25m coax cable and through the corresponding filters to ensure a good transfer, the signal arrives at the Control-and-Down-Conversion (CDC) board. On this board the Radio Frequency (RF) signal with all frequencies between 500 and 1500 MHz is mixed down in frequency by use of two Local Oscillators (LO). The first LO_1 has a frequency that can be set between 1400 and 2600 MHz. This shifts the signal to a 100 MHz band centered around 3000 MHz. The second LO_2 has a frequency that is $f_{LO2} = 2850$ MHz, which shifts the signal down to a band centered at 150 MHz, from 100 to 200 MHz (Bianchi et al. 2009). The actual value of f_{LO1} can be used to select what 100 MHz from the 1000 to 1500 MHz is mapped to the 100 to 200 MHz band. This 100 MHz wide band will be separated in 512 subbands in the digital part. It should be noted that the the input frequency range is from 1000 to 1500 MHz, because significant RFI in Europe is in the band from 500 to 1000 MHz.

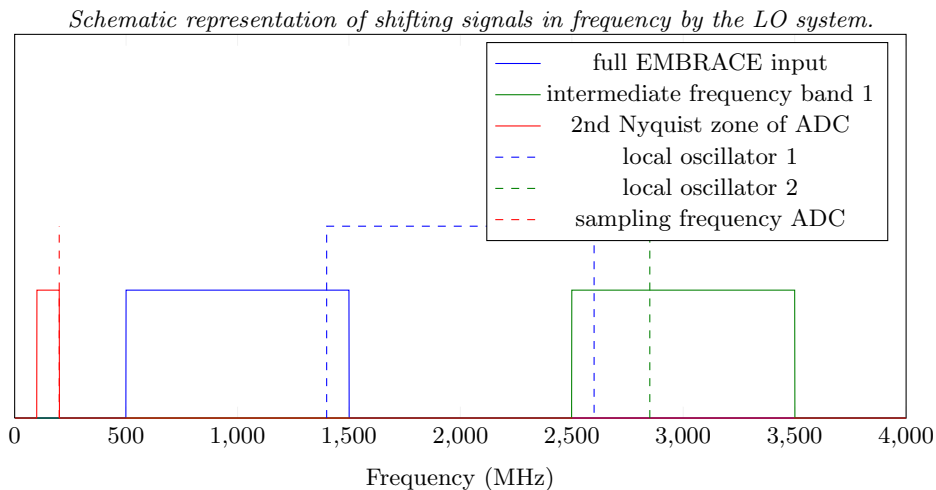


Figure 3.2: Shifting in frequency by local oscillators to select a 100 MHz band from the available input frequencies.

3.1.2 Digital Path

Right after the LO system on the CDC board, the signal is digitized by an Analog-to-Digital Converter (ADC) which is on a Remote Control Unit (RCU) board. The ADC has a frequency of $f_s = 200\text{MHz}$, so the first Nyquist band goes from zero to 100 MHz and the second one goes from 100MHz to 200MHz. It is the full second Nyquist zone that is used by the ADC to digitize the signal $x(t)$ every $T_s = \frac{1}{f_s}$, seconds. Through this the signal is quantized to integer voltages:

$$x[n] = Q(x(nT_s)) \quad n = 0, 1, \dots, N_{\text{samples}} \quad (3.1)$$

This digitized, quantized signal goes to a filter bank, where a combination of low-pass filters and mixers splits the signal in subbands.

$$s_j[n] = h_{LP}[n]x_j[n] \quad (3.2)$$

Consequently, there will be a filter response in every subband (more about filter responses in an upcoming section). After this filter H , there are 512 subbands s_0 to s_{511} . Of these subbands, 247 can be selected. It is also possible to select a single subband multiple times, but the maximum is 247. As visible in Figure 3.1, the beamlets are then exchanged between polarizations to make all the Stokes parameters. But since EMBRACE processes only a single polarization, this will not be used. The digital weights are applied and then the corresponding subbands of all tiles are added to form a set of EMBRACE beamlets (so called ebeamlets):

A beamlet is the signal from a specific position on the sky and in a specific frequency subband.

The four capture machines collect the ebeamlets. The user will decide what happens to the ebeamlets, the possibilities are

- no further operations: send the data to the user;
- correlations of the ebeamlets;
- apply N-point discrete Fourier Transform (NFFT).

3.1.3 Frequency Selection Control

Besides setting the geometrical delay and the weights, the user may want to set the selection of frequencies. The selection of frequencies from all the available frequencies is done in two steps. The user can give a command that sets the frequency of the first local oscillator f_{LO1} via the tileserver, such that the central frequency f_b from the RF will end up in a specified subband s_b . In the digital part, at ‘select’ in Figure 3.1, the frequency subbands are selected to become beamlets b . This selection is done by defining a map,

$$\begin{bmatrix} s_0 \\ s_1 \\ \vdots \\ s_b \\ \vdots \\ s_{511} \end{bmatrix} \xrightarrow{\text{map}} \begin{bmatrix} b_0 \\ b_1 \\ \vdots \\ b_{247} \end{bmatrix}.$$

The map contains the indices of the subbands and of the beamlets.

3.1.4 Control of Data Processing

The capture machines can send the collected ebeamlets via the network to the user, but it is also possible to further process them. One can make the capture machines do cross-correlations of the ebeamlets, by specifying another map. For example a map with the indices of the ebeamlets for two auto-correlations and one cross-correlation,

$$\text{map} = \begin{bmatrix} 0 & 0 & 1 \\ 0 & 1 & 1 \end{bmatrix} \Rightarrow \begin{cases} r_{0,0}[l] = \sum_{n=0}^{1024} b_0[n]b_0[n-l] \\ r_{0,1}[l] = \sum_{n=0}^{1024} b_0[n]b_1[n-l] \\ r_{1,1}[l] = \sum_{n=0}^{1024} b_1[n]b_1[n-l] \end{cases} . \quad (3.3)$$

The exact nature of the ebeamlets (selection of spatial and spectral details) give meaning to these correlations.

Besides this, the capture machines can also transform the correlated ebeamlets to the frequency

domain by a NFFT. The definition of the Discrete Fourier Transform (DFT) for an infinite number of values for ω is

$$X(e^{i\omega}) = \sum_n b[n]e^{-i\omega n}. \quad (3.4)$$

The number of values for ω should be a finite number, so

$$\omega_k = \frac{2\pi k}{N_{samples}} \quad k = 0, 1, \dots, N_{samples} - 1, \quad (3.5)$$

where $N_{samples}$ is the number of samples in a single ebeamlet. Then the NFFT will be for $N_{samples}$ values

$$\begin{aligned} X(e^{i\omega_k}) &= \sum_n b[n]e^{-i\omega_k n} \\ &= \sum_{n=0}^{N_{samples}} b[n]e^{-i2\pi kn/N_{samples}}. \end{aligned} \quad (3.6)$$

3.2 Pointing the Array and Gain Calibrations

On the right part of Figure 3.1, a simplified impression of the controlling parts of EMBRACE is shown. A user that runs a MATLAB session locally, can use different classes that are specifically written for this. The functions in these classes can control EMBRACE via the Local Area Network (LAN). As an example, the geometrical delays per tile can be calculated by a function and these results are sent to the HEX boards via the tile server. Furthermore, the digital weights per beamlet can be controlled by means of the rsp server. In the end, these servers can be controlled by the beam server, but it is still possible to connect to the tile and rsp server separately. The delays that are calculated by the functions are based on the theoretical geometrical delays \mathbf{w} (as in Equation (2.16)). If there are errors in the system, then the tiles should be calibrated. This can be done with a flux calibrator. When the tile beams are pointed to a bright point source, one can correlate the signals x from two antenna elements, e.g.

$$r_{1,2}(\tau) = \langle x_1(t)x_2(t - \tau) \rangle, \quad (3.7)$$

One should select a correct map and weights in order to make correlations between all tiles. The results can be put in the covariance matrix $\hat{\mathbf{R}}$,

$$\hat{\mathbf{R}} = \begin{bmatrix} r_{0,0} & r_{0,1} & \cdots & r_{0,N_{tiles}} \\ r_{1,0} & r_{1,1} & \cdots & r_{1,N_{tiles}} \\ \vdots & \vdots & \ddots & \vdots \\ r_{N_{tiles},0} & r_{N_{tiles},1} & \cdots & r_{N_{tiles},N_{tiles}} \end{bmatrix} = \hat{\boldsymbol{\nu}} \cdot \hat{\boldsymbol{\nu}}^H \quad \text{and} \quad \mathbf{R} = \mathbf{w} \cdot \mathbf{w}^H, \quad (3.8)$$

$\hat{\mathbf{w}}$ contains the experimentally determined values,

$$\hat{\boldsymbol{\nu}} = \begin{bmatrix} e^{-i\mathbf{k} \cdot \mathbf{r}_1} e^{i\epsilon_1} \\ e^{-i\mathbf{k} \cdot \mathbf{r}_2} e^{i\epsilon_2} \\ \vdots \\ e^{-i\mathbf{k} \cdot \mathbf{r}_{MN}} e^{i\epsilon_{MN}} \end{bmatrix}, \quad (3.9)$$

where $e^{i\epsilon_1}$ depicts the error with respect to the theoretical determined value $e^{-i\mathbf{k} \cdot \mathbf{r}_1}$. This error needs to be estimated in order to correct for it. The implemented self-referencing algorithm is based on Weighted Alternating Least Squares (WALS) (Wijnholds and van der Veen 2009) (Wijnholds and van der Veen 2010) and finds the error that minimises

$$\sum_{k,l} \left| \mathbf{R}_{k,l} - e^{i(\epsilon_k - \epsilon_l)} \hat{\mathbf{R}}_{k,l} \right|^2. \quad (3.10)$$

3.3 Filter Responses

Besides the calibration of tiles, also other corrections should be applied to reduce the effect of instrumental effects. One of this is the effect of using filters. There are two filters in the EMBRACE system: an analog filter and a digital filter. First the analog filter will be discussed, the digital filter will be discussed afterwards.

3.3.1 Filter Response for Data Transfer

The response of the first filter should be as flat as possible. This filter is applied over the total frequency range of EMBRACE, so inspection of it will include all subbands. Dion Kant has inspected this by sweeping LO_1 over subband 0 to subband 512, while pointing on a geostationary satellite. The result is shown in Figure 3.3. The left panel indeed shows a nearly flat transfer. When one makes a zoom in the right panel, one sees that the response varies by a few decibels.

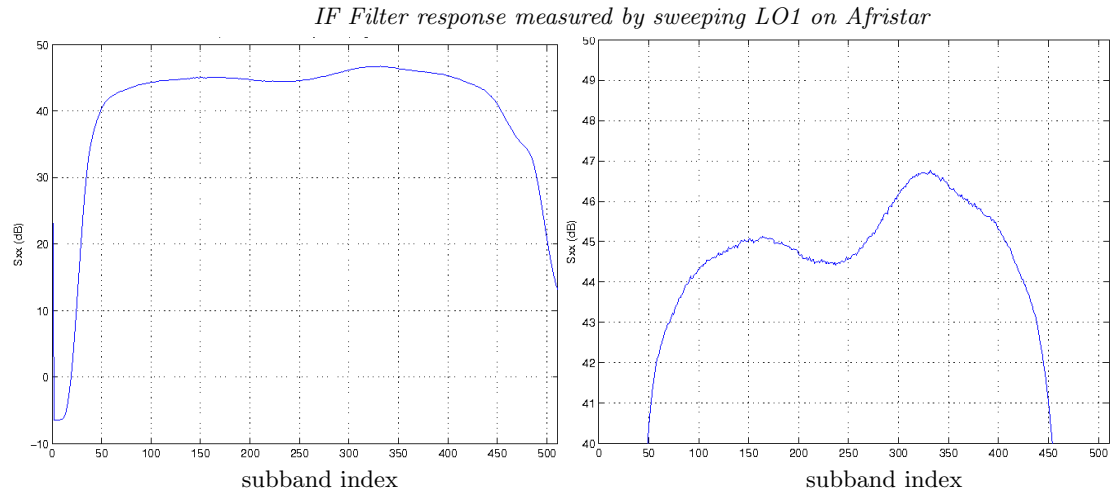


Figure 3.3: Filter response due to the filters for data transfer over the complete frequency range for a single tile: (*left*) complete response on a linear scale and (*right*) zoom on the flattest part on a dB scale (this test was done by Dion Kant).

3.3.2 Filter Response per Subband

Theory

There are two important filters in the data processing, one to ensure good transfer of signals to the ADC through the coax cables and one to split the frequency axis in subbands.

The second filter is used to split the subbands, so its response will be visible in every subband. This filter is a low-pass filter, which has a theoretical function of (Mitra 2006)

$$h_{LP}[n] = \sum_{n=-K}^K \begin{cases} \frac{\omega_{cut}}{\pi} & \text{for } n = 0 \\ \frac{\sin(\omega_{cut}n)}{\pi n} e^{-i\omega n} & \text{for } n \neq 0 \end{cases} \quad (3.11)$$

Where ω_{cut} is the angular cutting frequency. Using the design specifications for the values, this transfer is shown in Figure 3.4.

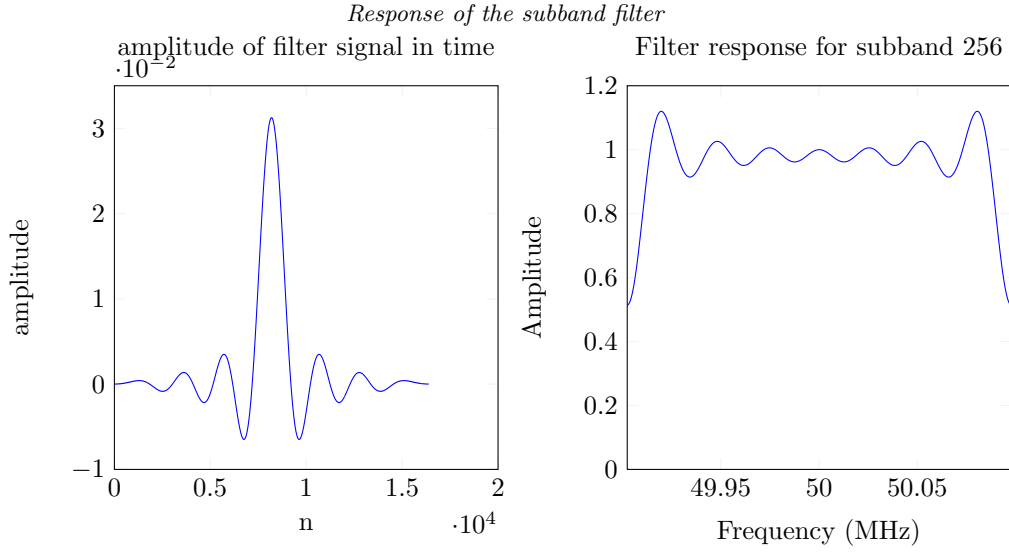


Figure 3.4: Response of the filter that splits the frequency axis into subbands: (*left*) the time signal and (*right*) in Fourier transform.

Filter Response Determination by Self-Generated Signals

The analog part of the data path can be ignored when the waveform generators are used, see Figure 3.1. It is possible then to inspect the digital part in more detail. For example the filter response of the filter that makes the subbands. The waveform generators (see Figure 3.5) will be used to generate a digital sinusoid of a specific frequency. For the 256th subband, the central frequency and the sampling frequency are given by

$$f_c = 50.00\text{MHz}, \quad f_s = 0.1953\text{MHz} \quad (3.12)$$

$$\begin{aligned} \Rightarrow f_{low} &= f_c - \frac{f_s}{2} = 49.90\text{MHz} \\ \Rightarrow f_{high} &= f_c + \frac{f_s}{2} = 50.01\text{MHz}. \end{aligned} \quad (3.13)$$

Such that for the frequencies f with $f_{low} < f < f_{high}$, the filter response is visible. The spectrum should peak at the chosen f and its amplitude will follow the filter response when f goes from f_{low} to f_{high} . This is exactly how the filter response is determined: spectra for a couple of measurements are shown in Figure 3.6 (*left*) and in Figure 3.6 (*right*) the resulting filter response is given.

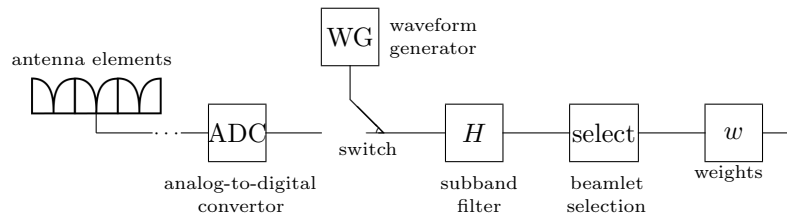


Figure 3.5: Signal path for measurements to determine the filter response by using waveform generators.

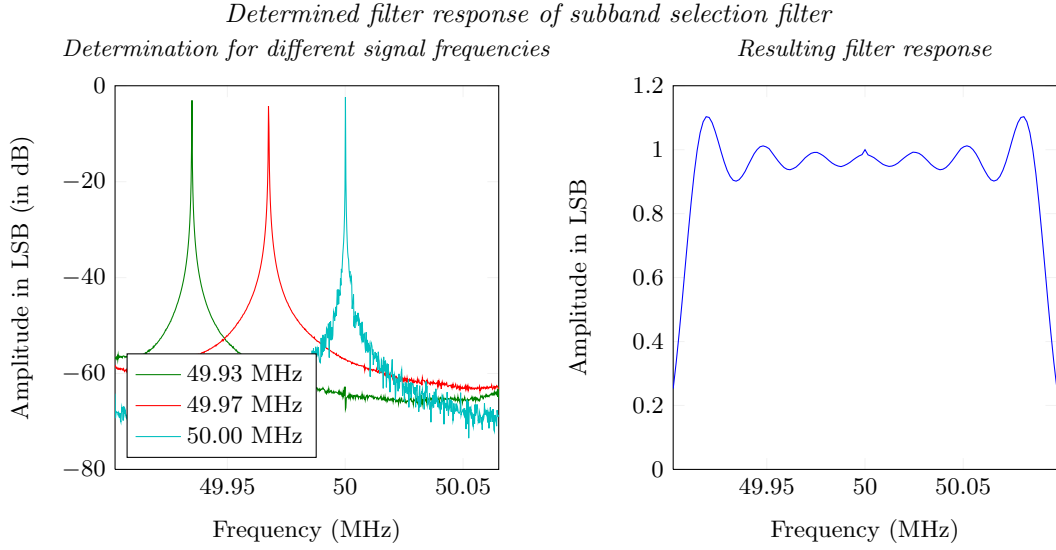


Figure 3.6: (left) Spectra of signals from the waveform generator with different frequency. For frequencies from low to high in this plot, the amplitude of the peak will follow the filter response. (right) The resulting filter response on a linear scale.

Filter Response Determination by Observation of Galactic HI

Another way to determine this filter response which also includes the analog part of the data path, is by doing an observation of the HI radiation. On 10 January 2013 at 16:37:30, the galactic HI was observed and the raw data contain the effect of the filters.

The raw data for a single pointing are shown in Figure 3.7 (left), which clearly contains a recurring filter response that divides the spectrum into subbands. By using a median over the subbands that do not contain Radio Frequency Interference (RFI) or flux from the HI line, the filter response can be determined empirically. The median operation is chosen, to reduce the effect of outliers. The result in Figure 3.7 (right) shows in general a good estimation of the filter response.

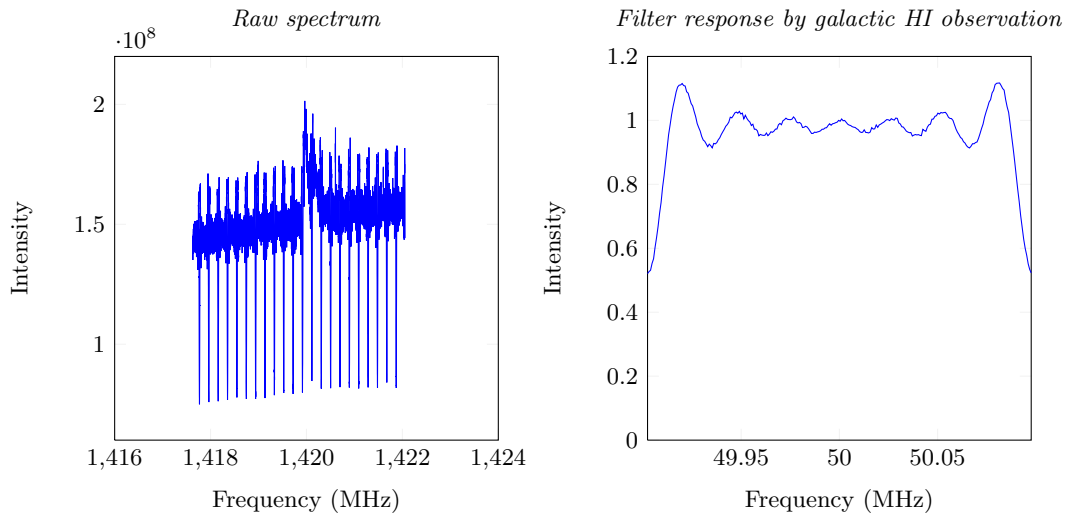


Figure 3.7: (*left*) Raw data from an observation of galactic HI on 10 January 2013 at 16:37:30: the filter response of the digital filter is clearly visible, as is the spectral line from HI. (*right*) The resulting filter response, using a median operation on noise-filled subbands.

3.3.3 Correction to the Digital Filter Response

Now that the digital filter response is modelled and determined, it is possible to compare the results. Figure 3.8 shows the results. There are some minor differences visible between the result from waveform generators and from the HI observation. This may be due to the fact that the determination using waveform generators only uses the digital data path, while the other determination uses both the analog and the digital data path. When the model is used for correction, the spectrum from 3.7 (*right*) becomes the one in figure 3.8 (*right*).

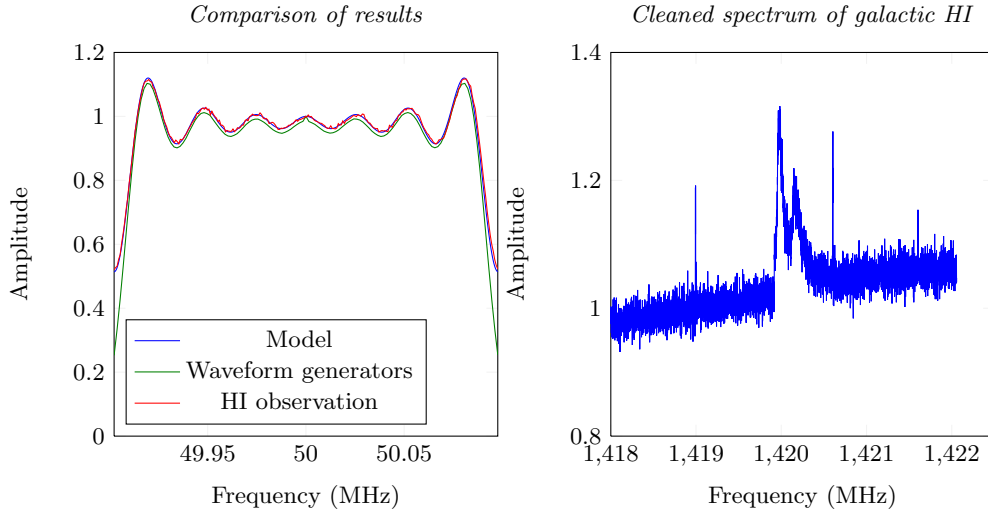


Figure 3.8: (left) Comparison of modelled and empirically determined results for the digital filter. (right) The corrected spectrum (corrected by the model). At the edge of each subband is a peak visible, due to the division by a very small number.

3.4 Performance of an Expanding Array

During this thesis work, the array was expanded from 60 to 98 tiles. In order to check the larger array, a check of the individual tile gains and their calibration was required.

3.4.1 Frequency Measurements of a Geostationary Satellite

The response of a tile can be examined using the known spectrum of the Afristar satellite which is visible from Westerbork. The satellite is positioned in a geostationary orbit at $(\theta, \phi) = (61.9^\circ, 147^\circ)$ and emits 6 beams towards the Earth (see Table 3.1). The frequencies are in EMBRACE’s observing range, so the flux of the beams from Afristar should be visible when a power spectrum is made. Dion Kant tested this by making 98 times a power spectrum of Afristar. First all tiles are shutted down and each time a power spectrum is made, a new tile is reactivated. As such, the collecting area is increased and it is expected that the power should increase by 3 dB for each doubling of collecting area.

The result from this test is shown in Figure 3.9: the first three large peaks are the beams 1, 2 and 3 of Afristar. They are not directly emitted towards Dwingeloo, but the frequencies are matching. The fourth beam is not intense, which can be explained by the fact that the polarization may be in EMBRACE’s Y polarization. Combining this with the fact that the emission is towards the southern hemisphere makes this beam barely detectable with EMBRACE. The two beams that are pointed in the direction of Dwingeloo, are the most intense and even overlap. Since not a single spectrum is off, one can conclude that the large grid is working as expected.

Beam	TP	Polarization	Frequency (MHz)
East	1	Right	1469
East	2	Left	1471
South	3	Left	1473
South	4	Right	1475
West	5	Left	1488
West	6	Right	1490

Table 3.1: Emission specifications of the Afristar satellite.

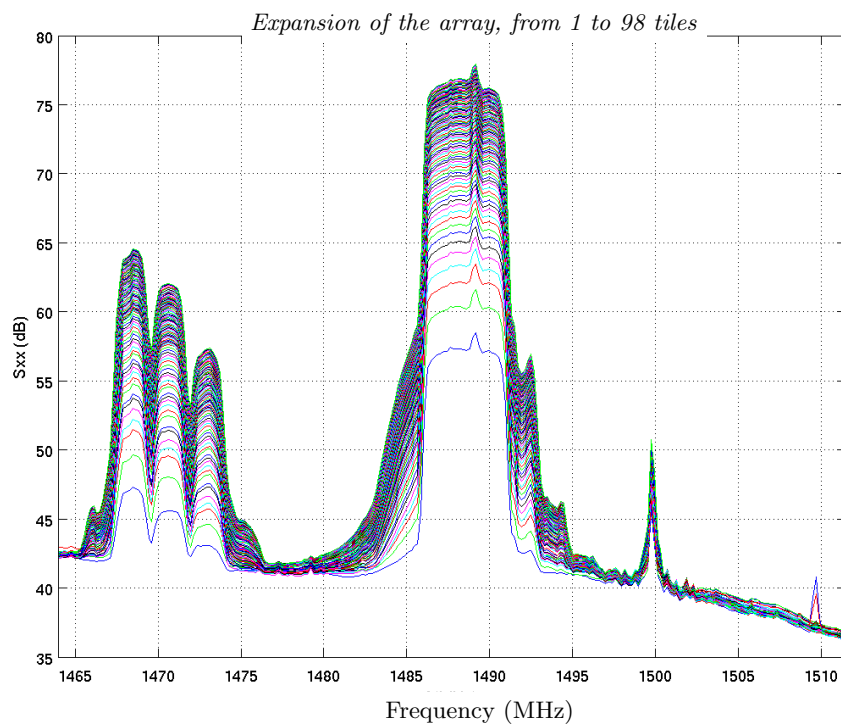


Figure 3.9: Increase of the gain for increasing number of tiles when pointing towards the Afristar satellite.

Chapter 4

FRINGE MEASUREMENTS

4.1 Correlations and Fringe Measurements

For radio astronomy, the use of EMBRACE will be interesting if some specific measurements can be done. The focus in the upcoming sections is on making fringe measurements.

For a monochromatic point source with frequency ω that goes over two antennas, one can correlate the responses. E.g.

$$r_{x,y}(\tau) = \langle x(t)y(t - \tau) \rangle. \quad (4.1)$$

τ is a time delay. If it is zero one can rewrite this equation to

$$\begin{aligned} r_{x,y}(0) &= \langle x(t) \cdot y(t) \rangle \\ &= \langle G_x(t)s(t) \cdot G_y(t) \cos(\omega\tau_g)s(t) \rangle, \end{aligned} \quad (4.2)$$

since the same wavefront $s(t)$ will be recorded by the antennas with gains G_x and G_y , where the wavefront has been corrected for the geometrical delay. By $\tau_g = b \sin(\theta(t))$, this becomes

$$r_{x,y}(t) = G_x(t)G_y(t)s^2(t) \cos(\omega b \sin(\theta(t))). \quad (4.3)$$

The cosine factor in Equation (4.3) is called the fringe function of an interferometer. The equation is for the perfect case that a point source has a trajectory that is in the same direction as the baseline. Within the array it is possible to select different baseline orientations. To incorporate this, the projected angle θ' needs to be taken into account. This is depicted in Figure 4.2. The projection of the trajectory onto the baseline orientation will affect the fringe function via θ' :

$$\theta(t) = \cos(\beta)\theta'(t).$$

For constant gains, the absolute behaviour of the fringe function with projected angle θ' is shown in Figure 4.1 (*top*). The discussion in the previous section yields that the antenna gains are not constant for EMBRACE. It depends on the actual position of the source with respect to positions of the elements. In order to correlate two tile beams, the AP of a tile are used as the gain for the antennas. Figure 4.1 (*bottom*) shows this effect for a tile beam. Fringe measurements like this can be done to inspect whether EMBRACE is working fine and calibrated correctly. Figure 4.1 shows the absolute values of the complex fringe pattern. When the fringe pattern is plotted in the complex plane, one will see a circular behaviour around zero in the perfect case. This is depicted in Figure 4.3.

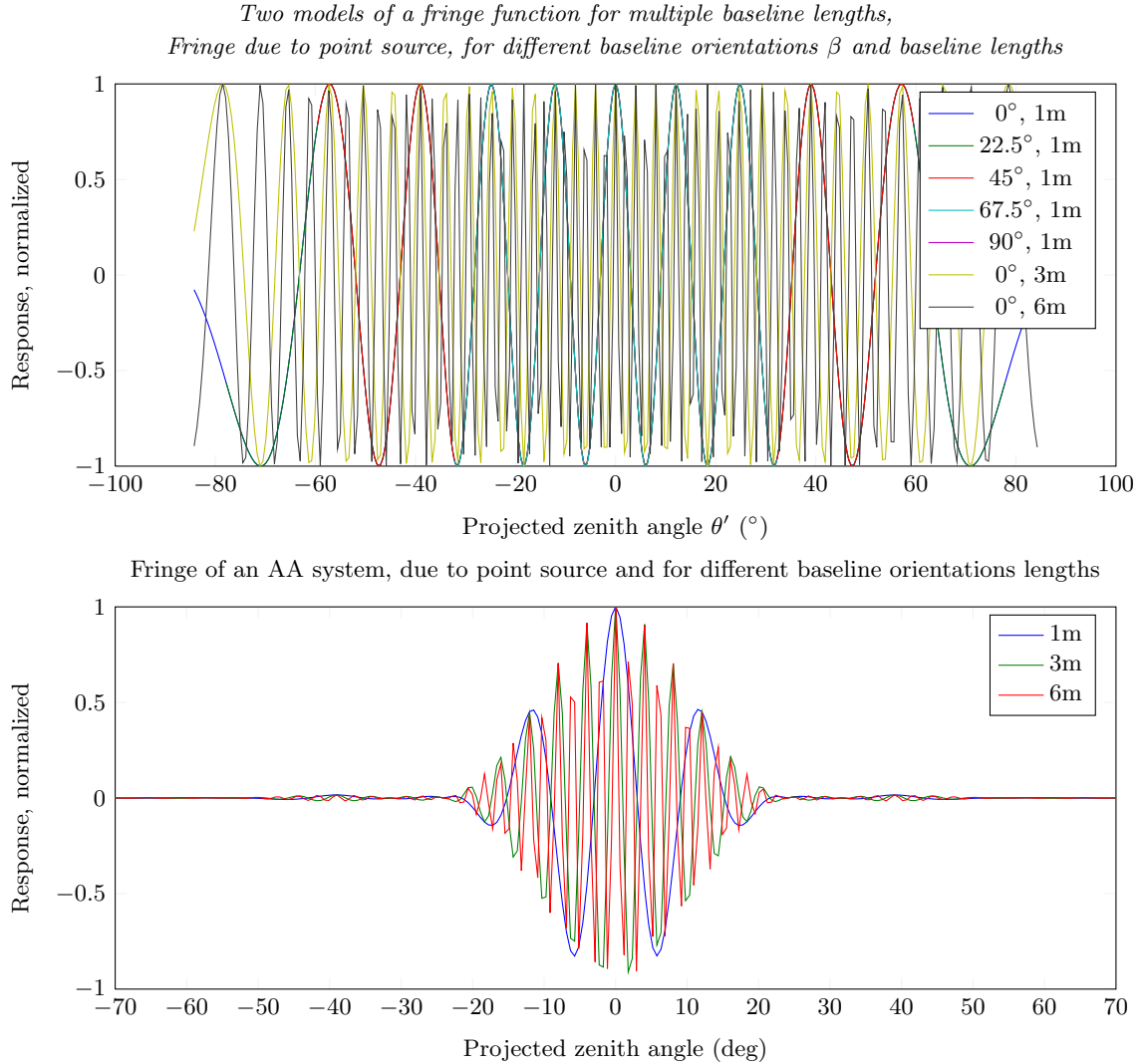


Figure 4.1: (*top*) Simplified model of fringes due to a monochromatic point source, for gain factors that are independent on sky position, for different baseline lengths b and for different angles β between source trajectory and baseline orientation. For constant b and increasing β the curve spans a smaller range in projected zenith angle, as can be expected from Figure 4.2. For increasing b and constant β , the fringe rate goes up with the same rate. (*bottom*) For gain factors that represent the antenna pattern of an EMBRACE tile, an envelope becomes visible. This envelope is due to the sinc behaviour of the AP, as can be seen in Figure 2.6.

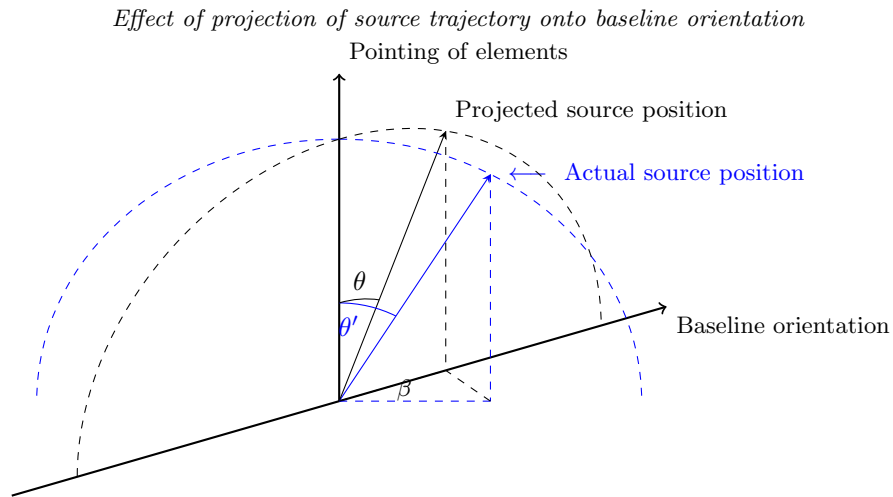


Figure 4.2: For a point source with a trajectory that matches the baseline orientation (the black trajectory), there is no projection effect. If it does not match (the blue trajectory), the projected θ' onto the baseline orientation will be smaller than the actual angle between pointing and source position.

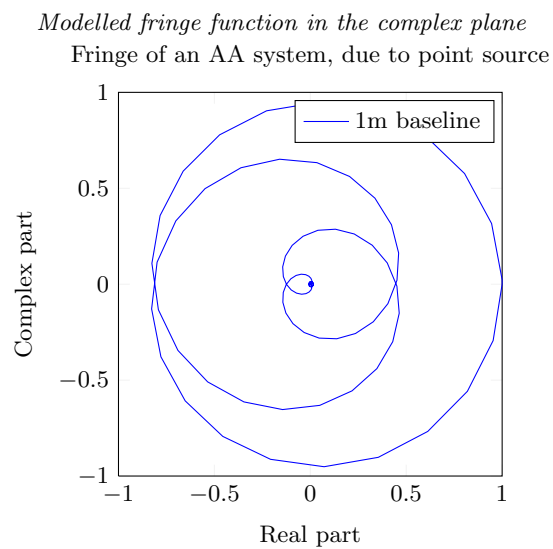


Figure 4.3: In the ideal case, the complex fringe function has a circular behaviour.

4.2 Fringe Measurements on Stars and Satellites

With the 98 tiles in the WSRT station, it is possible to test EMBRACE using fringe measurements. The large array brings some flexibility: many different baseline orientations and lengths can be selected.

On 9 March 2013 at 15:34:17 a non-tracking fringe measurement of 1 hour of the highest GPS satellite at that moment (satellite ‘BIIA-28 (PRN 08)’) is done for a frequency of 1228 MHz (integration time was 30 seconds). Later, on 10 March 2013 at 17:16:23 and on 11 March 2013 at 22:35:56 fringe measurements of Cas A at 1401.5 MHz were done. The first time for 4 hours, the second time for 3 hours (integration time was 60 seconds). Figures 4.4 and 4.5 show the real part of the fringes for respectively the GPS and the Cassiopeia A (Cas A) measurements. The expectation from the previous section that the fringe rate goes up with the same rate as the baseline length b (for the same orientation) holds in the fringe measurement of the GPS satellite. For example the cyan and purple baselines have the same orientation, but their ratio of baseline lengths is

$$\frac{b_{cyan}}{b_{purple}} = \frac{8}{4} = 2. \quad (4.4)$$

In Figure 4.4 (*bottom*) that same ratio in fringe ratio can be seen after analysis.

For the measurements on Cas A, the trajectories are also given. It is possible to see the influence of the different baseline orientations on the fringe pattern. In the top panel of Figure 4.5 one sees that the fringe pattern has a larger fringe rate for the blue baseline. This baseline is parallel to the trajectory of Cas A. On the other hand, the cyan colored fringe pattern has the projection effect and is therefore barely a fringe pattern.

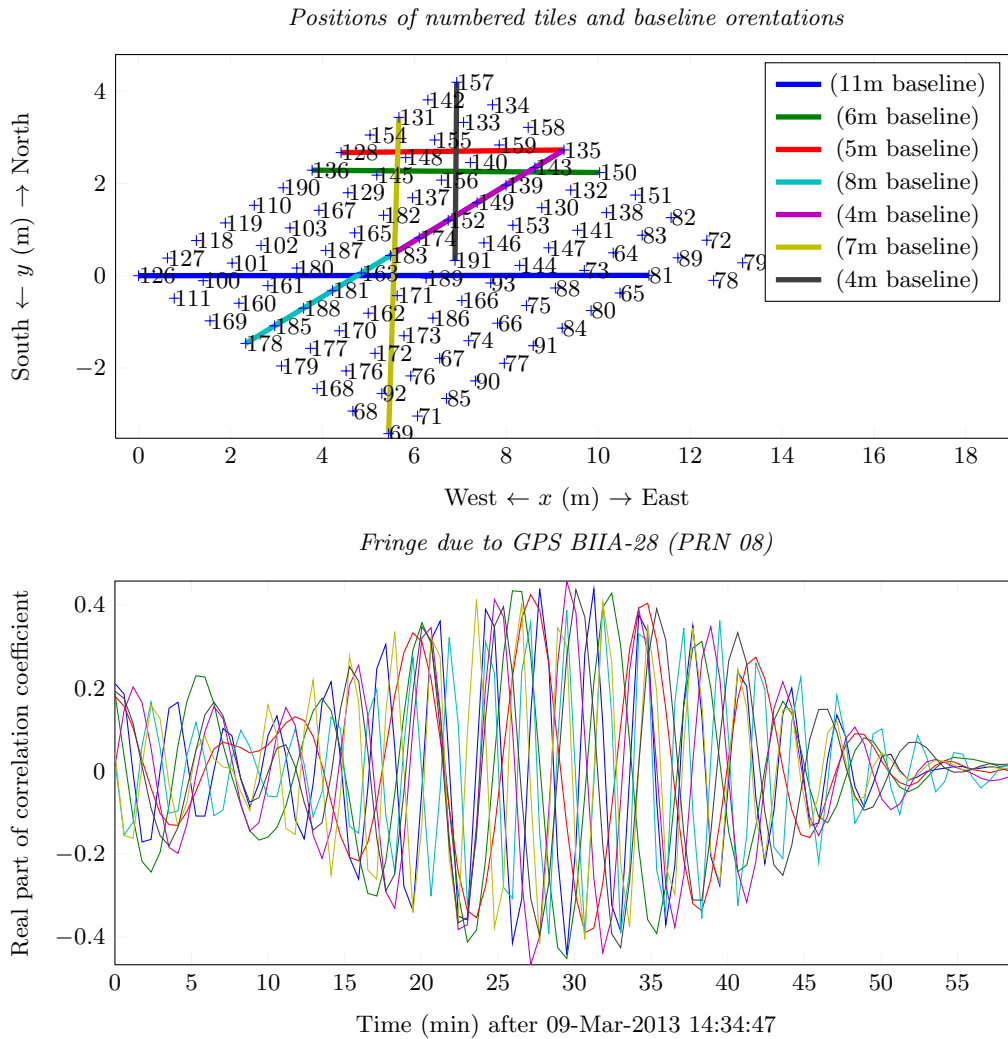


Figure 4.4: (*top*) Baseline length and orientations that are used in this and the other figures of this chapter. (*bottom*) Real part of the fringe due to a GPS satellite.

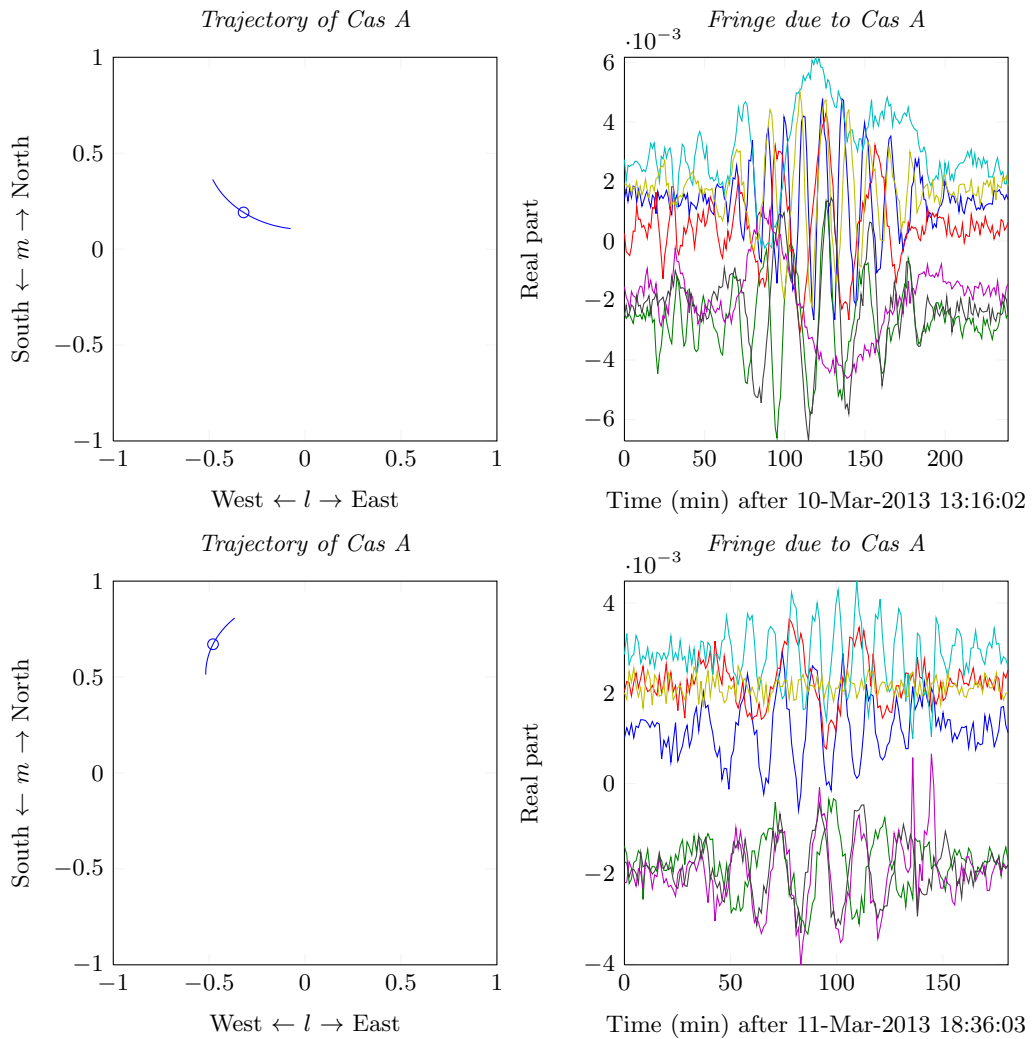


Figure 4.5: The top row shows the fringe measurement on 10 March: (*left*) the trajectory of Cas A during the observation. The circle shows where the array was pointed to; (*right*) The real part of the correlation coefficient. The lower panels show the fringe measurement on 11 March

4.3 Correlator Offset and Correction

The vertical offset for some of the fringe patterns in the previous section is even more clear when they are shown in the complex plane. Figure 4.6 shows the complex fringes of the satellite and the Cas A observations. This offset is due to instrumental effects, namely the correlator offset. It would be interesting to see whether this instrumental effect is constant with time, that's why there is a second Cas A observation. There is a pause of approximately 1 day between the lower panels in Figure 4.6. The displacement of the complex fringe patterns (for example the red one), shows that the offset is not constant with time. However, during the timespan of a single observation, the offset is more or less constant. As such, it is possible to correct for the offset per observation by subtracting the median of a fringe pattern in both the real and complex part. The result in Figure 4.7, shows that this works quite well.

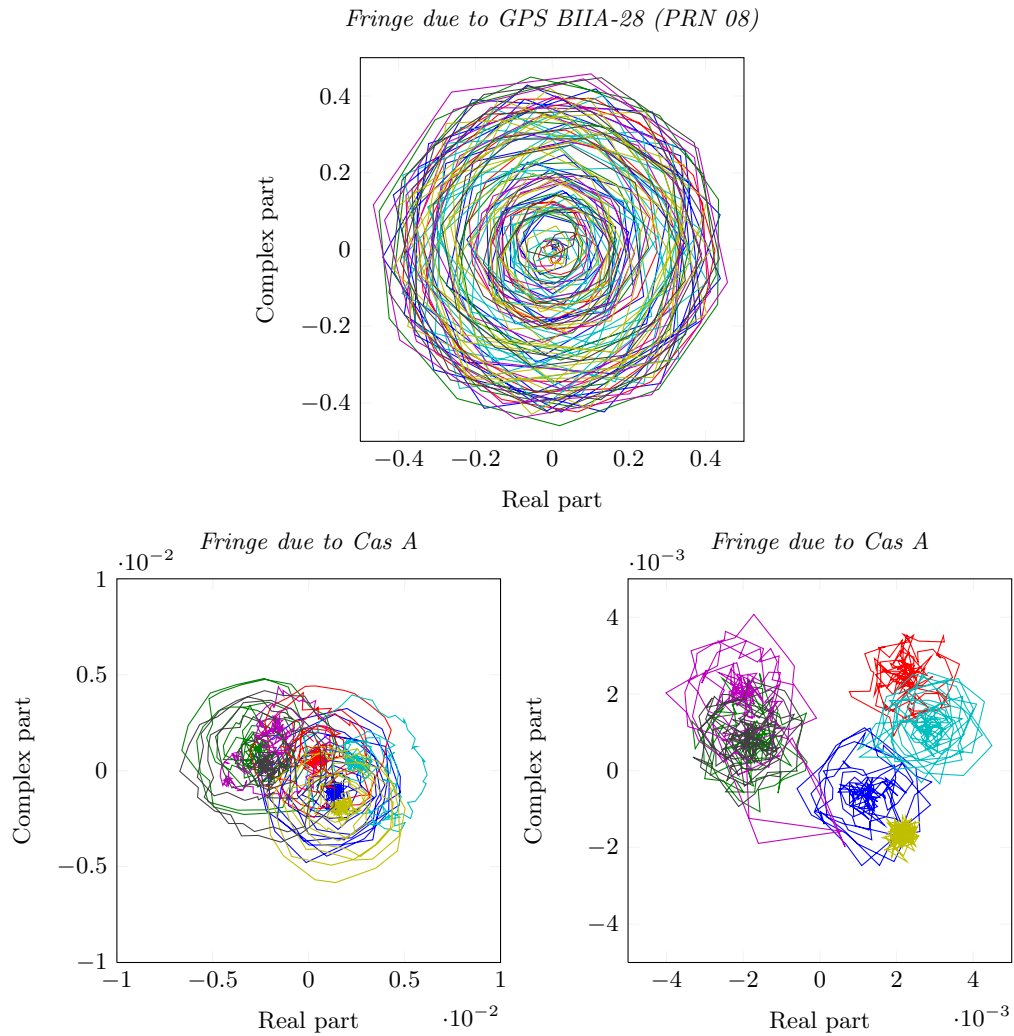


Figure 4.6: Complex fringes of (*top*) a GPS satellite, (*left*) Cas A on 10 March 2013 and (*right*) Cas A on 11 March 2013.

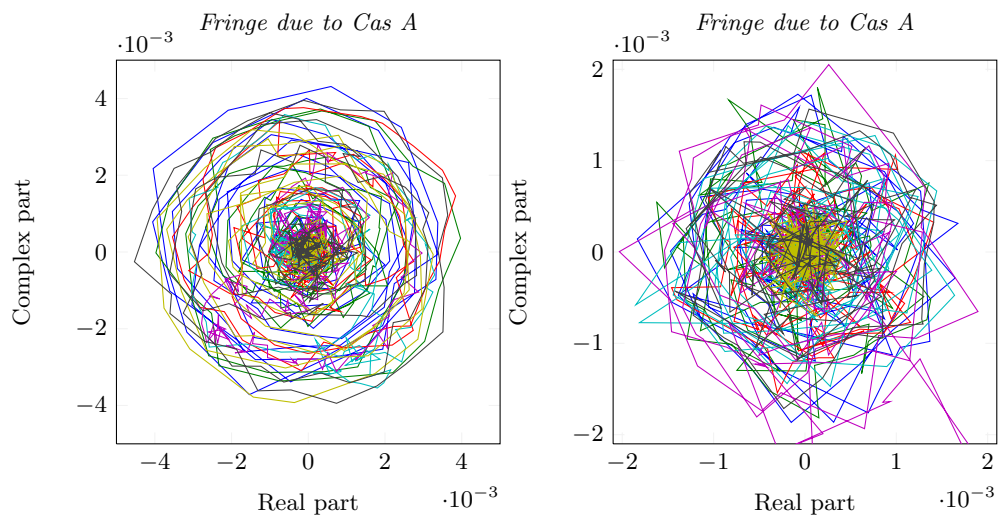


Figure 4.7: Corrected complex fringes for the Cas A measurements on (left) 10 March and (right) 11 March.

Chapter 5

SYSTEM TEMPERATURE OF EMBRACE

In the analog data path are some Low Noise Amplifiers (LNAs) and coax cables. All the analog devices add noise to the system. This system noise is represented by the system temperature T_{sys} and is added to the signal that comes from the source of interest, e.g.

$$T_{measured} = T_{antenna} + T_{sys}. \quad (5.1)$$

Where $T_{measured}$ is the total temperature that is measured by the system and $T_{antenna}$ is the temperature that comes from the source of interest.

The system temperature is a figure of merit. Knowing the value for EMBRACE would give insight in the total system performance. For the smaller array of 88 tiles, the system temperature was measured by the Sun, on a frequency of 1.4 GHz. The resulting T_{sys} was somewhere between 103 and 117 K (Wijnholds et al. 2009), quite close to the design goal of 100 K (Kant et al. 2011). In this chapter, the system temperature is measured using two independent methods. First T_{sys} is determined by fringe measurements of Cas A and later by observations of galactic HI.

5.1 T_{sys} Determination by Fringe Measurements on Cassiopeia A

The fringe measurement on CasA from the previous chapter can be used to determine the system temperature. To obtain such good fringes, calibration of the array was required. Furthermore, the measurements were corrected for any offsets and the result in Figure 4.7 show the amplitude of the envelope clearly. This amplitude relates to the sensitivity by (Wijnholds et al. 2009)

$$\frac{A_{eff}}{T_{sys}} = \frac{2k_b}{S_{CasA}} \frac{P_{CasA}}{P_n + P_{CasA}}. \quad (5.2)$$

Where $k_b = 1.38 \cdot 10^{-23} \text{ WK}^{-1}\text{Hz}^{-1}$ is the Boltzmann constant, S_{CasA} is the flux of CasA, P_n is the system noise power and P_{CasA} is the power received from CasA and $\frac{A_{eff}}{T_{sys}}$ is a measure of sensitivity. For known S_{CasA} (Baars et al. 1977) which is corrected by the fading rate (Reichart and Stephens 2000) and A_{eff} of a tile that accounts for the zenith angle of the position of Cas A,

$$\begin{aligned} A_{eff} &= 1.125\text{m}^2 \cdot \cos(\theta) \\ S_{CasA} &= 1876.5\text{Jy} \pm 2\%, \end{aligned}$$

one can measure the latter fraction of (5.2) for both observations of Cas A to deduce T_{sys} . Subscript 1 denotes the observation on March 10 and subscript 2 denotes the observation on March

11.

$$\begin{aligned}
\theta_1 &= 21.79^\circ \\
\left(\frac{P_{CasA}}{P_n + P_{CasA}} \right)_1 &= (4.3 \pm 0.2) \cdot 10^{-3} \\
\Rightarrow T_{sys,1} &= 165 \pm 9 \text{ K}
\end{aligned} \tag{5.3}$$

$$\begin{aligned}
\theta_2 &= 57.97^\circ \\
\left(\frac{P_{CasA}}{P_n + P_{CasA}} \right)_2 &= (2.2 \pm 0.2) \cdot 10^{-3} \\
\Rightarrow T_{sys,2} &= 188 \pm 33 \text{ K}
\end{aligned} \tag{5.4}$$

(5.5)

Where the standard deviation of T_{sys} are calculated using the rules of error propagation. Furthermore, the 2% error on S_{CasA} is taken into account as an one sigma error.

5.2 T_{sys} Determination by Spectra from Galactic HI

Another way to determine T_{sys} is using the known HI temperatures from the LDS data. In this way, the galactic neutral hydrogen acts as an intensity calibrator. Figure 5.1 (*left*) shows the spectrum from EMBRACE, for the galactic coordinates $(b, \ell) = (2.0, 93.3)$. The observation was done on 4 February 2013 at 12:56:25 and the integration time was 21 seconds. The intensity offset I_{off} is the contribution of the system noise, I_{on} is the intensity at the frequency where the HI profile is.

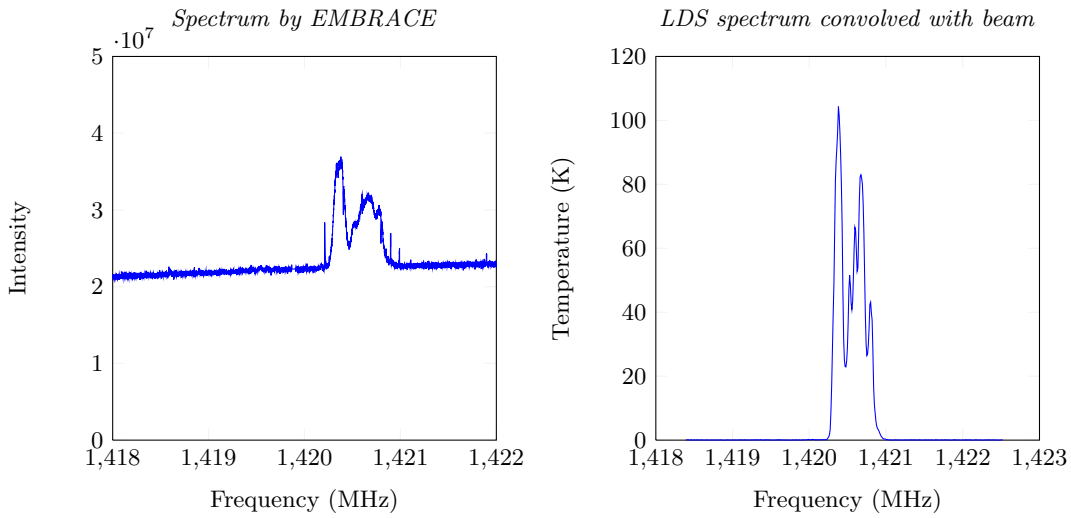


Figure 5.1: Spectrum of the HI line (*left*) from EMBRACE and (*right*) the EMBRACE beam convolved with LDS data.

5.2.1 Spectra of Galactic HI by the Leiden-Dwingeloo Survey

The LDS data contains also spectral information of the galactic HI emission. This data is given in temperatures, so it can function as a calibrator of the measured intensities by EMBRACE. For the black circles in Figure 1.2, the LDS spectra are given in Figure 5.2. From both figures, it is clear that this radiation is most intense for the region with small galactic latitude values. There is only a small region where this radiation is more intense, that is in the direction of the center of the Milky Way ($\ell \sim 0$ and $b \sim 0$).

For the galactic coordinate of the abovementioned observation, the spectrum from the LDS is convolved with the beam of that moment (see Figure 5.1 *right*). More about this convolution method will be in the next chapter, for now it is sufficient to mention that the result of this convolution can be used as an expectation of the spectrum by EMBRACE. From the Figures, one can get the expected observed HI temperature $T_{HI} = 100 \pm 5$ K, $I_{off} = 2.2 \pm 0.1$ and $I_{on} = 3.7 \pm 0.1$. Using

$$\begin{aligned}
 T_{sys} &\simeq T_{HI} \frac{I_{off}}{I_{on} - I_{off}} \\
 &= 100 \pm 5 \text{ K} \cdot 1.46 \\
 &= 146 \pm 10 \text{ K}
 \end{aligned}$$

Again, the error in T_{sys} is determined according to the rules of error propagation.

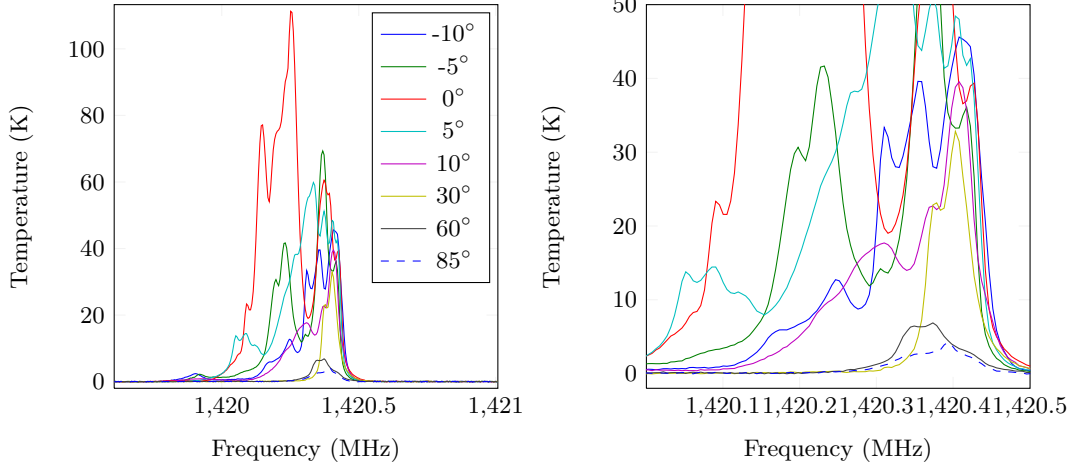
Spectra of atomic hydrogen for different galactic latitudes from LDS along galactic longitude of 150° 

Figure 5.2: Frequency distribution of the 21 cm line for $\ell = 150^\circ$ and $b = \{-10^\circ, -5^\circ, 0^\circ, 5^\circ, 30^\circ, 60^\circ, 85^\circ\}$. This data is taken from the LDS, which has a average standard deviation of $\sigma_T = 0.07\text{K}$. The right panel is a zoom on the left panel. The positions are also shown in Figure 1.2.

5.3 Comparison of Results for T_{sys}

The different methods in the previous sections have different results. The two fringe measurements at 1402 MHz yields two system temperatures of

$$\begin{aligned} T_{sys,1} &= 165 \pm 9 \text{ K} \\ T_{sys,2} &= 188 \pm 33 \text{ K}. \end{aligned}$$

The result from the HI observation is

$$T_{sys,3} = 146 \pm 10 \text{ K}.$$

Now the goal at 1 GHz was 100 K. Since these measurements were all done around 1.4 GHz, it is expected that the system temperature from these measurements will be higher than 100 K. Since the results in this thesis are consistent, a weighted mean will be applied to come to a final value for T_{sys} and its standard deviation:

$$\begin{aligned} T_{sys} &= \frac{\frac{165}{9^2} + \frac{188}{33^2} + \frac{146}{10^2}}{\frac{1}{9^2} + \frac{1}{33^2} + \frac{1}{10^2}} \\ &= 157 \pm 7 \text{ K}. \end{aligned} \tag{5.6}$$

Chapter 6

OBSERVING ASTRONOMICAL SOURCES

Besides correlating, EMBRACE can be used to make spectra and maps of astronomical sources. To do so, there are multiple aspects that become important. First of all, some words on tile and array beams. The second section is about the trade off between integration time and sensitivity. Combining the LDS data with the EMBRACE beam, it is possible to make a prediction of the EMBRACE spectra. A comparison with the actual EMBRACE spectra is made in the third section.

6.1 Tile and Array Beams

For a single tile, the collecting area is

$$\begin{aligned} A_{eff}^{1 \times 1} &= A_{phys} \\ &= 1.125 \text{m}^2 \end{aligned} \quad (6.1)$$

Using the equation that the HPBW is approximated by

$$\theta \simeq \frac{k\lambda}{D}, \quad k \sim 1 \quad (6.2)$$

Then for a single tile and $\lambda = 0.2111\text{m}$,

$$\begin{aligned} \Rightarrow \theta_{1 \times 1} &\simeq 0.2111 \text{rad} \\ &= 12.10^\circ. \end{aligned} \quad (6.3)$$

Then the solid angle of the tile beam is

$$\begin{aligned} \Omega_{1 \times 1} &= \left(\frac{\theta_{1 \times 1}}{2} \right)^2 \pi \\ &= 114.9 \text{sqdeg}. \end{aligned} \quad (6.4)$$

This is the beam that is pointed by the geometric, analog delays. The beam that is the result of the digital weights is the array beam. The EMBRACE array that is in the configuration of Figure 2.4 (*second row, left*) has 8×12 tiles. The collecting area is larger, so the solid angle of this beam is smaller, e.g.

$$A_{eff}^{8 \times 12} = 8 \cdot 12 \cdot A_{phys} = 108.0 \text{m}^2, \quad (6.5)$$

$$\begin{aligned}
\Rightarrow \theta_{8 \times 12} &\simeq \frac{0.2111\text{m}}{\sqrt{12\text{m} \cdot 8\text{m}}} \\
&= 0.02155\text{rad} \\
&= 1.234^\circ,
\end{aligned} \tag{6.6}$$

$$\begin{aligned}
\Rightarrow \Omega_{8 \times 12} &= 1.196 \text{ sqdeg} \\
&< \Omega_{1 \times 1}.
\end{aligned} \tag{6.7}$$

So it is possible to make multiple array beams within a single analog pointing. The array beams can be used to sample within the analog beam and can be used to make a map of the sky within $\Omega_{1 \times 1}$ by only pointing the tiles once.

However, there is a limiting factor in all this: the backend can only process a total bandwidth of 48.4375 MHz per single pointing. A trade-off between the spatial and spectral coverage will be needed. As such, the spectra in this chapter is created using a single array beam and thus with the widest possible frequency range.

6.2 Integration Time and Sensitivity

Since the sensitivity in the spectra is the rms noise on the measured data values according to

$$\sigma_S = \frac{2kT_{sys}}{A_{eff}\sqrt{B\tau}}. \tag{6.8}$$

Where τ is the observation time, B is the bandwidth of the observation, T_{sys} is the system temperature and k is the Boltzmann constant. Equation (6.8) can be used to find a practical optimum between σ_S and the integration time per pointing. Theoretically, the sensitivity would be best when $\tau = \infty$, but that would be a bit unpractical. Equation (6.8), is verified here and can be used to determine a practical balance between integration time and sensitivity. For multiple values of τ and for a single subband (subband 150) the standard deviation is determined. The result is in Figure 6.1. From the figure, one can conclude that for integration times longer than 180 seconds, the sensitivity does not improve significantly. σ_S goes down very much in the first 100 seconds. In the rest of this chapter, the integration time is set to 180 seconds.

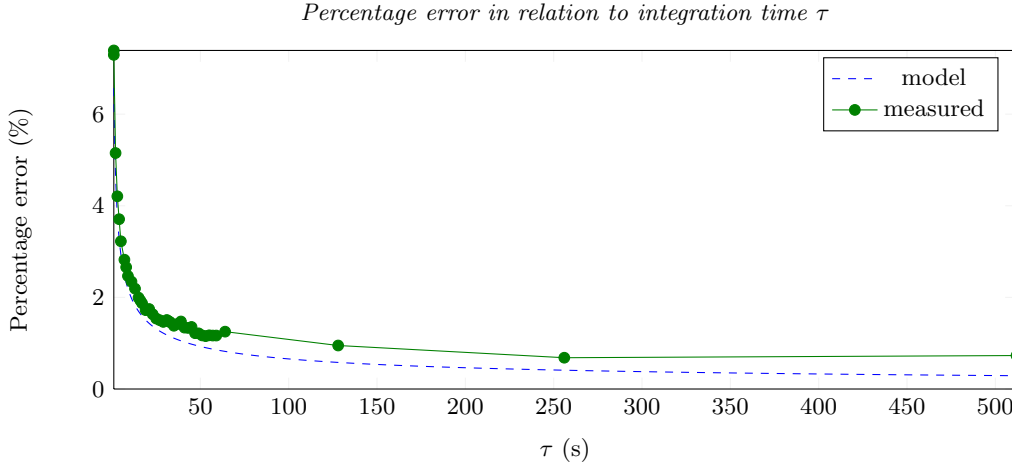


Figure 6.1: Determined sensitivity on spectral values for different integration times τ .

6.3 Convolution of Leiden-Dwingeloo Survey Data

The LDS data can be used as a sky model, to make a prediction for an EMBRACE observation. In this section, the theoretical background is given.

From antenna theory (Kraus 1986), the received power in Watt of an antenna with effective area A_{eff} in m^2 and dimensionless normalized antenna response P_n from a brightness distribution B is given by

$$P = \frac{1}{2} A_{\text{eff}} \int_{\nu}^{\nu+\Delta\nu} \iint_{\Omega} B(\theta, \phi) P_n(\theta, \phi) d\Omega d\nu, \quad (6.9)$$

where ν is a frequency in Hz, $\Delta\nu$ is a finite bandwidth in Hz, Ω is the solid angle in steradian, $B(\theta, \phi)$ is the brightness of the sky in $\frac{\text{W}}{\text{m}^2 \text{Hz sr}}$ at position (θ, ϕ) in the Horizon coordinate system, $d\Omega$ is an infinitesimal solid angle of sky in steradian and $d\nu$ is an infinitesimal bandwidth in Hz. Then the total source flux density S is defined as

$$S = \iint_{\text{source}} B(\theta, \phi) d\Omega, \quad (6.10)$$

where S is in $\frac{\text{W}}{\text{m}^2 \text{Hz}}$ or in janski ($1\text{Jy} = 10^{-26} \frac{\text{W}}{\text{m}^2 \text{Hz}}$) and the integral is over the solid angle of the source.

Now the observed flux density can be expressed as

$$S(\tilde{\theta}_0, \phi_0) = \iint_{\text{source}} B(\gamma, \phi) \tilde{P}_n(\gamma_0 - \gamma, \phi_0 - \phi) \cos(\tilde{\theta}) d\tilde{\theta} d\phi, \quad (6.11)$$

where $\tilde{P}_n(\tilde{\theta}_0 - \tilde{\theta}, \phi_0 - \phi) = P_n(\tilde{\theta} - \tilde{\theta}_0, \phi - \phi_0)$ and $\tilde{\theta} = 90^\circ - \theta$.

Equation (6.11) is called the convolution and can be rewritten as

$$S = B * \tilde{P}. \quad (6.12)$$

So to make an prediction for an EMBRACE observation, a sky model should be convolved with the antenna pattern. Data from the LDS can be used for the sky model and the antenna pattern is given in a previous chapter. Figure 6.2 shows what the prediction of an EMBRACE observation will look like, according to the above-mentioned approach.

The spectrum in Figure 5.1 (*right*) is made by convolving the sky model B , per frequency bin. The intensities from the LDS data are integrated, so that a single sky model has the same frequency

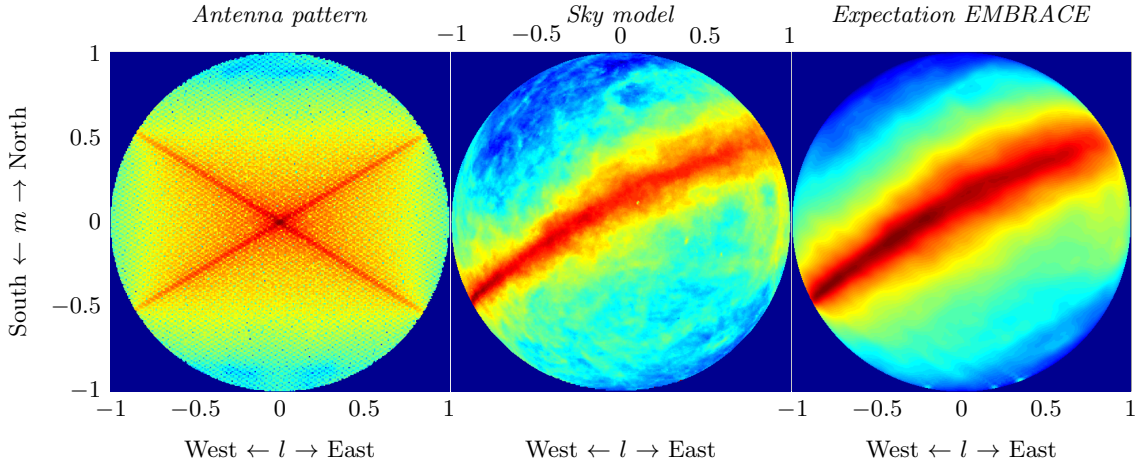


Figure 6.2: Expectation of an EMBRACE observation, by convolving LDS data as a sky model with the EMBRACE antenna pattern. The plots are presented on a logarithmic scale, to see the effect on the filamentary structure. Grating lobes are not taken into account here.

range. Figure 6.3 shows the effect of convolution by an array beam, in respect to the original LDS observation of the HI line. The sizes of the array beam ($\theta_{8 \times 12} = 1.234^\circ$) and the Dwingeloo Telescope beam ($\theta_{DT} = 0.5^\circ$) are comparable. Consequently, the difference between the LDS observation and the one that is convolved with the EMBRACE array beam is small.

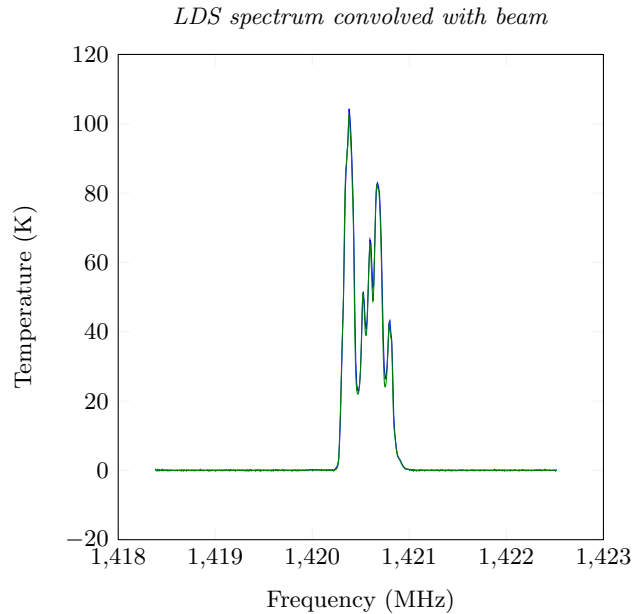


Figure 6.3: Effect of the convolution, (blue) LDS observation for $(b, \ell) = (2.0^\circ, 93.3^\circ)$, (green) result convolution by observation on 4 February 2013 at 12:56:25.

6.4 Spectra by EMBRACE

For multiple galactic coordinates, EMBRACE is used to make spectra of galactic HI emission.

6.4.1 Data Reduction

The data that is captured during the observation is only corrected for instrumental effects. Baseline subtraction will give a spectrum of the HI line profile only, so further data reduction is needed. For a raw spectrum from the dataset (as in Figure 6.4), first very sharp peaks are removed by using a threshold that is based on the local median value. Afterwards, a polynomial is fitted to the continuum. This fit is then subtracted from the original spectrum, such that there is only flux from the HI line left.

Another spectrum by EMBRACE is processed this way and scaled to match the convolved LDS spectrum. Accordingly, a comparison from the result (see Figure 6.5) shows that the EMBRACE spectra are of good quality.

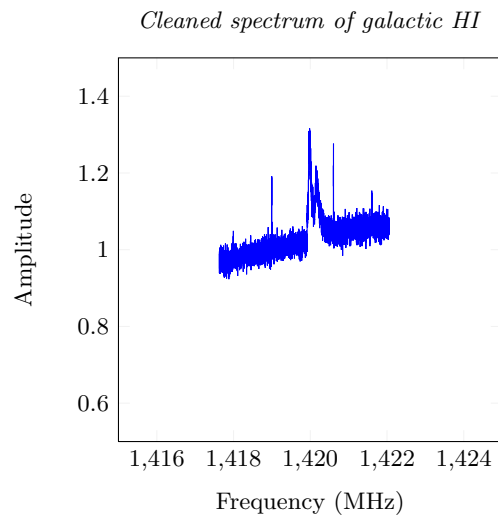


Figure 6.4: Spectrum observed by EMBRACE. There is data reduction needed, in order to get the HI line only.

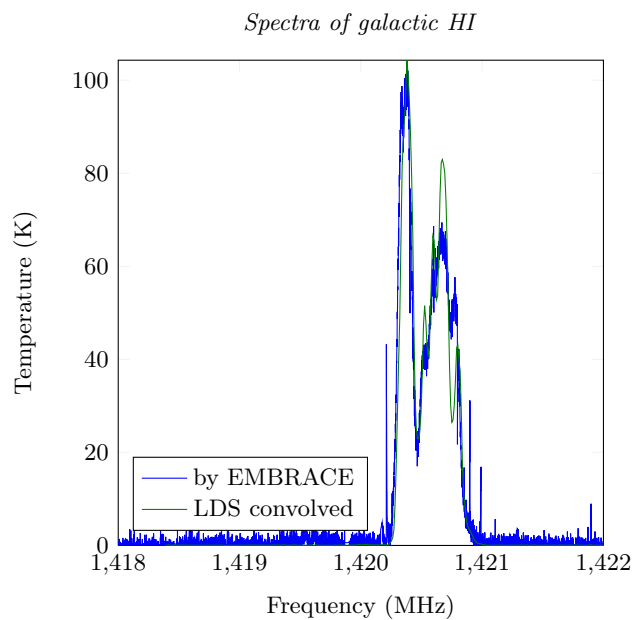


Figure 6.5: Comparison of spectrum by EMBRACE and the LDS data, convolved with the EMBRACE array beam.

Chapter 7

CONCLUSIONS AND FUTURE WORK

In this thesis, many aspects of AA technology have been presented. The theoretical background was discussed. The EMBRACE WSRT station has been used for testing to characterize the system and to show the capabilities of EMBRACE. This thesis work tries to answer the main question: Can AA technology produce data of scientific quality at the SKA mid/AA frequencies?

First of all, instrumental effects are important when it comes to the production of scientific data. The data from EMBRACE contain filter responses from the analog and digital filters. It is shown that this fingerprint can be removed quite well. Only near the edges of each subband, a sharp peak appears.

Furthermore, fringe measurements were done to inspect offsets in the complex plane, and more importantly, to measure the system temperature. For two fringe measurements that were done with a one day interval, it was clear that the offsets were shifted, so that they are variable with time. On the other hand, the complex fringes clearly rotated around a specific point. This indicates that during a single measurement of 4 hours, the instrumental effect is constant and can be corrected for.

A well known figure of merit is the system temperature. The system temperature of EMBRACE is determined in two independent ways, both at a frequency of 1.4 GHz. Fringe measurements yields 165 ± 9 K and 188 ± 33 K. Observations of galactic HI emission yield 146 ± 10 K. The system was designed to have a system temperature of 100 K at a frequency of 1 GHz. Since the results shown in this work are at a higher frequency, it was expected that the results should be above the 100 K. At 1 GHz, earlier work showed that the EMBRACE system has a system temperature of 103 and 117 K at the design frequency, which is also a bit above the desired 100 K. From this, the values that are shown in this work seems to be plausible for the frequency of 1.4 GHz. In the end, the system temperature for EMBRACE at 1.4 GHz will be $T_{sys} = 157 \pm 7$ K.

In the end, EMBRACE was used to make spectra of galactic HI emission. The spectra that are presented show good correspondence with the ones measured with the Dwingeloo Telescope.

7.1 Future Work

To extend the knowledge about EMBRACE, more observations can be done. For example more fringe measurements can be done to inspect the behaviour of the offset in the complex plane. It will be insightful to see how this works, since it may help to further develop and perfect the EMBRACE system. Because EMBRACE is designed to correlate the stations, it will be interesting to perform a fringe measurement using both the Nançay and WSRT station.

It is also possible to do more independent measurements of the system temperature, for example by measuring the black body radiation that comes from the moon. The known temperature of the moon can then be used to calibrate the measured intensities to temperature. It will also be interesting to see what the system temperature is at other frequencies than 1 and 1.4 GHz.

Broadband emission from Cas A or Cygnus A could be used to get this information. Another important goal for EMBRACE would be to make maps of galactic HI emission. First, a map can be made by a single array beam. In the end it would be interesting to use more array beams in a single tile beam, at the cost of the frequency range. Reducing the frequency range by a factor of two, makes it possible to also reduce the observation time by this factor. Consequently, it would be possible to make maps much faster and then the power of AA technology as part of SKA mid really comes strong.

Chapter 8

ACKNOWLEDGEMENTS

This master research has been done with the help of many people. I would like to thank all of them. In particular my supervisors, Thijs van der Hulst, Arnold van Ardenne and Stefan Wijnholds who made it possible to do a research in the interesting field of astronomical instrumentation. Then I would like to thank the EMBRACE team at ASTRON for their help and support: Dion Kant, Pieter Benthem, Ilse van Bemmelen, Erik van der Wal, André Gunst, Leon Hiemstra and Mark Ruiter. They explained things that were not clear at once and I believe that the interaction in this group made it possible to improve EMBRACE and get the results that are presented in this work.

I would also like to thank all the people that I could join for travel from and to Dwingeloo: Stefan, Maura, Elizabeth, Tom, Carmen, Rik, Adriaan, Marco and Alex. In the end I would like to thank the people working in the ASTRON building in general. Being surrounded by all these nice people made it fun to be in Dwingeloo during these seven months.

References

- The Astronomical Almanac for the Year 2012, 2012.
- J. W. M. Baars, R. Genzel, I. I. K. Pauliny-Toth, and A. Witzel. The absolute spectrum of CAS A - an accurate flux density scale and a set of secondary calibrators. *A&A*, 61:99–106, October 1977. doi: 10.1086/146760.
- G. Bianchi, J. Morawietz, S. Mariotti, F. Perini, M. Schiaffino, and G. W. Kant. EMBRACE Local Oscillator distributor. In Torchinsky et al., editor, *Wide Field Astronomy & Technology for the Square Kilometre Array*, 2009. ISBN: 978-90-805434-5-4.
- A. Blaauw, C. S. Gum, J. L. Pawsey, and G. Westerhout. Note: Definition of the New I.A.U. System of Galactic Co-Ordinates. *ApJ*, 130:702, September 1959. doi: 10.1086/146760.
- B. F. Burke and F. Graham-Smith. *An Introduction to Radio Astronomy*. Cambridge University Press, third edition edition, 2010. ISBN: 978-0-521-87808-1.
- R. M. Green. *Spherical Astronomy*. Cambridge University Press, 1993. ISBN: 0-521-31779-7.
- D. Hartmann and W. B. Burton. *Atlas of Neutral Hydrogen*. Cambridge University Press, 1997. ISBN: 0-521-47111-7.
- G. W. Kant, P. D. Patel, S. J. Wijnholds, M. Ruiter, and E. van der Wal. EMBRACE: A Multi-Beam 20,000-Element Radio Astronomical Phased Array Antenna Demonstrator. *IEEE Transactions on Antennas and Propagation*, 59:1990–2003, June 2011. doi: 10.1109/TAP.2011.2122233.
- J. D. Kraus. *Radio Astronomy*. Cygnus-Quasar Books, 2nd edition edition, 1986. ISBN: 978-1-882484-00-3.
- S. K. Mitra. *Digital Signal Processing - A Computer-based Approach*. McGraw-Hill, third, international edition, 2006.
- D. E. Reichart and A. W. Stephens. The Fading of Supernova Remnant Cassiopeia A from 38 MHz to 16.5 GHz from 1949 to 1999 with New Observations at 1405 MHz. *ApJ*, 537:904–908, July 2000. doi: 10.1086/309073.
- SKA Organisation. The Square Kilometre Array. <http://www.skatelescope.org/>, January 2013.
- S. J. Wijnholds and A.-J. van der Veen. Multisource Self-Calibration for Sensor Arrays. *IEEE Transactions on Signal Processing*, 57:3512–3522, September 2009. doi: 10.1109/TSP.2009.2022894.

-
- S. J. Wijnholds and A.-J. van der Veen. Self-Calibration of Radio Astronomical Arrays With Non-Diagonal Noise Covariance Matrix. March 2010. 17th European Signal Processing Conference (EuSipCo).
- S. J. Wijnholds, G. W. Kant, E. van der Wal, P. Benthem, M. Ruiter, P. Picard, S. A. Torchinsky, S. Montebugnoli, and R. Keller. EMBRACE: First experimental Results with the Initial 10% of a 10,000 Element Phased Array Radio Telescope. In *Wide Field Astronomy & Technology for the Square Kilometre Array*, 2009.

Glossary

AA	Aperture Array.
ADC	Analog to Digital Converter.
ASTRON	Netherlands Institute for Radio Astronomy.
BF	Beam Former.
CDC	Control and Down Conversion.
DT	Dwingeloo Telescope.
EMBRACE	Electronic Multi-Beam Radio Astronomy Concept.
FoV	Field of View.
HPBW	Half-Power Beam Width.
IF	Intermediate Frequency.
LDS	Leiden-Dwingeloo Survey.
LNA	Low Noise Amplifier.
LO	Local Oscillator.
LSB	Lower Side Band.
NWO	Netherlands Organisation for Scientific Research.
RCU	Receiver Unit.
RF	Radio Frequency.
RFI	Radio Frequency Interference.
RSP	Remote Station Processor.
SKA	Square Kilometre Array.
WSRT	Westerbork Synthesis Radio Telescope.